Theoretical modeling of granular-fluid hopper flows

Marko Korhonen

School of Science

Thesis submitted for examination for the degree of Master of Science in Technology.

Espoo 24.10.2017

Thesis supervisor:

Prof. Mikko Alava

Thesis advisor:

D.Sc. (Tech.) Antti Puisto

Aalto University
School of Science

AALTO UNIVERSITY
SCHOOL OF SCIENCE

ABSTRACT OF THE
MASTER'S THESIS

Author: Marko Korhonen

Title: Theoretical modeling of granular-fluid hopper flows

Date: 24.10.2017 Language: English Number of pages: 6+48

Department of Applied Physics

Professorship: F-3005

Supervisor: Prof. Mikko Alava

Advisor: D.Sc. (Tech.) Antti Puisto

Sands, slurries and powders represent systems that consist of granular particles and are ubiquitous both in nature and in the industrial environment. Their flow behavior is of particular interest, since these materials are able to both bear external stress as solids and flow like fluids. These attributes are particularly conspicuous in a hopper flow, which is regularly encountered in industrial settings, where granular media is stored and tranported in these hoppers/silos. In this type of flow, the orifice of a hopper filled with granular particles is opened, and the granular particles exit the hopper via the orifice under the stress imposed by gravitation. As a result, the hopper empties. Theoretically, these flows have been primarily modeled in dry conditions, and typically, any interactions between the granular particles and the surrounding air are ignored. In such a setting, the Beverloo equation has great predictive power over the granular discharge rate. However, in recent experimental work involving hoppers submerged in a liquid, the Beverloo equation is unable to account for the observed results. Therefore, this work aims to provide theoretical results matching the ones produced in these experiments and offer a coherent description of the surge (acceleration) of the granular discharge rate that is retrieved in the experimental work. The approach adopted here is to model the submerged, filled hopper as a two-phase system, in which the liquid phase is modeled on a continuum level using Computational Fluid Dynamics (CFD), while the granular phase is described as discrete particles by the Discrete Element Method (DEM). By modifying and applying a fluid-particle interaction term to the underlying equations in these methods, the experimental results are well matched by the simulations. Additionally, it is demonstrated that the surge is a result of an effective pumping induced by the exiting granular particles, which is a direct consequence of the condition imposed by the first Navier-Stokes equation on the flow fields.

Keywords: Granular media, Multiphase flow, Hopper flow, CFD, DEM

AALTO-YLIOPISTO
PERUSTIETEIDEN KORKEAKOULU

DIPLOMITYÖN
TIIVISTELMÄ

Tekijä: Marko Korhonen

Työn nimi: Raesuspension siilovirtauksen teoreettinen mallinnus

Päivämäärä: 24.10.2017 Kieli: Englanti Sivumäärä: 6+48

Teknillisen fysiikan laitos

Professuuri: F-3005

Työn valvoja: Prof. Mikko Alava

Työn ohjaaja: TkT Antti Puisto

Rakeisista partikkeleista koostuvat kokonaisuudet ovat monella tapaa läsnä arkipäiväisessä ympäristössämme ja niihin lukeutuvat niin luonnon hiekka kuin myös ruokateollisuuden erinäiset jauheet sekä pulverit. Näiden aineiden virtauskäyttäytyminen on erityisen rikasta, sillä ne voivat olosuhteista riippuen käyttäytyä joko kiteisen aineen tai nesteen tavoin. Tämä käytös tulee esille erityisesti ns. siilovirtauksissa, jotka ovat yleisiä teollisuuden sovelluksissa, joissa rakeisia aineita sekä säilytetään että siirretään erilaisten siilojen välityksellä. Kyseisessä virtaustyypissä täytetyn siilon pohjassa oleva oleva sulkuaukko avataan, jolloin rakeinen aine poistuu painovoiman vaikutuksesta sulkuaukon läpi, ja siilo tyhjenee. Teoreettisesti näitä virtauksia on mallinnettu tyypillisesti kuivissa olosuhteissa, jolloin rakeisen aineen mahdolliset vuorovaikutukset ympäröivän ilman kanssa jätetään usein huomiotta. Tällöin rakeisen aineen purkausnopeus on ennustettavissa ns. Beverloo-yhtälön mukaisesti. Viimeaikaiset kokeelliset tulokset ovat kuitenkin osoittaneet, että siilovirtauksen tapahtuessa ilman sijaan nesteessä ei Beverloo-yhtälö kykene selittämään havaittuja tuloksia tyydyttävästi. Tässä työssä tarkoituksena onkin toistaa laskennallisesti nämä kokeelliset tulokset sekä tarjota selitys tuloksissa havaitulle purkausnopeuden sysäykselle (kiihdytykselle). Työn mallinnuksen lähtökohtana nesteeseen upotettua, täytettyä siiloa kuvataan kaksifaasisysteeminä, jossa nestettä kuvataan jatkumotasolla laskennallisen nestedynamiikan (CFD) keinoin, ja rakeista faasia diskreetteinä partikkeleina (DEM). Näiden menetelmien perusyhtälöitä muokkaamalla voidaan rakeisen aineen ja nesteen vuorovaikutukset ottaa luontevasti huomioon, ja kokeelliset tulokset saadaan jäljiteltyä simulaatioissa hyvin. Lisäksi purkausnopeuden sysäyksen osoitetaan johtuvan pumppausvaikutuksesta, jonka siilosta poistuvat rakeiset partikkelit kohdistavat nestefaasiin, mikä on suora seuraus ensimmäisen Navier-Stokes-yhtälön asettamasta vaatimuksesta virtausolosuhteille.

Avainsanat: Rakeinen aine, Monifaasivirtaus, Siilovirtaus, CFD, DEM

Preface

I wish to thank D.Sc. Antti Puisto, D.Sc. Mikael Mohtaschemi and Prof. Mikko Alava for their excellent tutelage and support over the years and throughout this project. Their guidance and ideas for improvement have been indispensable for this work to be possible.

Otaniemi, 24.10.2017

Marko Korhonen

Contents

Symbols and abbreviations

Symbols

$\mathbf{u}$	Fluid phase – translational velocity
$\mathbf{v}$	Solid phase – translational velocity
$\mathbb{T}$	Stress tensor
p	Pressure
V	Volume
η_{fl}	Fluid viscosity
ρ_{fl}	Fluid density
ϵ_{fl}	Fluid volume fraction
$\mathbf{x}_p$	Position of the volume centroid
$\mathbf{x}_f$	Position of the face centroid
$\mathbf{S}$	Surface normal vector
$\mathbf{d}$	Relative displacement vector of two neighboring volume centroids
$g(r)$	The local averaging weighing function

Operators

:	Tensorial inner product, i.e. $a : b = \sum \sum a_{ij} b_{ji}$

Abbreviations

BD	Blended Differencing
CD	Central Differencing
CFD	Computational Fluid Dynamics
DEM	Discrete Element Method
FVM	Finite Volume Method
MCA	Minimum Correction Approach
MD	Molecular Dynamics
MPI	Message Passing Interface
OCA	Orthogonal Correction Approach
ORA	Over-relaxed Approach
PISO	Pressure Implicit with Splitting of Operator
UD	Upwind Differencing

1 Introduction

Sand, slurries and powders exemplify a class of materials known as *granular media* [1]. In these materials, the particles composing the system share a common attribute as their size exceeds that of one micrometer, and they can be dispersed in a surrounding medium [1]. While granular materials are *per se* of profound importance in many fields of industry, it is their flow behavior that is truly interesting for layman and researcher alike: many natural phenomena ranging from the common (flow of mud on a rainy day) to the spectacular (landslides, erosion [2]) capture fundamental qualities of granular flow. Indeed, accurate modeling of these flows is equally paramount to predicting these natural occurences as well as refining industrial processes associated with transporting and storing granular products [3].

From the modeling point of view, any theoretical framework should capture the quintessential features of a granular system and be readily implemented numerically. In this sense, granular materials possess numerous unique aspects. Due to their rather considerable particle size, thermal effects, such as Brownian motion can be generally neglected at normal temperatures [1, 3–5]. Additionally, attractive forces between neighboring particles are close to nonexistent and due to inelastic collisions and friction, the interparticle interactions tend to result in energy dissipating rapidly in the system [3, 5–8]. As such, a diverse range of models originating from statistical mechanics or microscopic and continuum approaches have been developed to mimic granular flow [4]. As these models can be mutually exclusive and usually limited to specific flow scenarios [4], the field can be described as fragmented at best. With all such intricacies, the validation and capabilities of the diverse computational model implementations have been tested in specific reference scenarios with well-established flow patterns, such as the granular discharge flows in a hopper geometry [9], a relevant model system due to its industrial significance [6, 10]. For instance, this geometry has been applied extensively in the food industry, where *e.g.* flour, tea and milk powders are stored and distributed in hoppers/silos [11, 12].

Indeed, despite the variety of the modeling approaches, the outflow of granular media from such containers is understood reasonably well. In such a flow, numerous quantities of interest can be monitored both experimentally and in theoretical simulations. These include the granular discharge rate Q_g, which refers to the mass (or volume) rate, at which the particles are exiting through the orifice. In the dry case, this quantity has been extensively verified to obey the empirical Beverloo equation [13, 14]

$$Q_g = C\rho_b g^{1/2}(D_0 - kd)^{5/2}, \tag{1}$$

where C and k are dimensionless fitting parameters, ρ_b is the bulk density of the granular phase, g is the gravity constant, D_0 is the orifice diameter and d is the particle diameter. Eq. 1 has been verified on a multitude of experiments, although strictly speaking, it applies only when $D_0 \gg d$ [14]. A remarkable feature resulting from Eq. 1 is that the discharge rate is independent of the filling height h, denoting the height of the packed granular bed inside the hopper. This is a clear distinction from a bed consisting purely of a (Newtonian) liquid, which would exhibit a monotonic decrease in its discharge rate as h decreases [15]. This behavior can be rationalized

with the concept of a free-fall arch, depicted in Fig. 1. This arch forms spontaneously above the orifice in a hopper flow as the granular media is exiting via the orifice. Physically, the arch corresponds to a boundary, above which the granular particles are effectively jammed due to their frictional interactions. Below the boundary, however, the particles are free to exit unhindered under the gravitational force [16–18]. As a result, the mean number and velocity of exiting particles remains constant, yielding a constant discharge rate. Although useful, this concept has been under considerable scrutiny, and some authors have suggested that the arch only serves as an approximation for a more continous transition between the stuck and free-fall areas [19].

In addition to the pure granular flows depicted above, granular-fluid flows are also recurring events in nature. Indeed, if the granular particles are embedded in an interstitial phase, such as a gas or a liquid, the resulting particle-gas or particle-liquid interactions have to be accounted for and the modeling aspects are affected accordingly. In these multi-phase flows, theoretical approaches seem to have focused on modeling the two phases separately and then fusing them together by mutual interaction terms [21]. As a recent development, the (microscopic) Discrete Element Method (DEM), first introduced by Cundall and Strack in their seminal work [22], has been used for modeling the granular phase, which is then coupled to the fluid phase, described either by continuum or microscopic equations [21, 23]. Interestingly enough, relatively little experimental (or theoretical) work has been accomplished with respect to granular-fluid flows even in simple reference systems, such as the hopper/silo geometry. Additionally, in the majority of the published articles, the interstitial fluid of choice is regularly a gas. Indeed, to the author's best knowledge, the recently issued experimental results by Durian *et al.* [13] provide the seminal work that characterizes the granular-liquid flow in a hopper that is completely submerged in a liquid. In the submerged hopper, the authors in Ref. [13] reported an intriguing result as they observed an unexpected increase (surge) in the granular discharge rate Q_g as the hopper emptied and h decreased. Thus, this behavior is completely different from the pure granular flow and the (Newtonian) liquid flow inside the hopper as discussed above, and prompts a vast array of questions. Since to date, no theoretical treatment of the granular-liquid flow in a hopper exists, this thesis aims to serve as a preliminary theoretical development and address some of the issues, such as the surging of the granular phase, directly.

Therefore, in this work, the hopper discharge flows of submerged granular particles is examined theoretically. First, the Navier-Stokes (NS) equations for a single phase fluid are examined and the Finite Volume Method (FVM) discretization, utilized by the Computational Fluid Dynamics (CFD) approach applied to fluid flow, is presented in the context of these equations. Then, by means of spatial local averaging as described in Ref. [24], the NS equations are extended to accomodate the granular phase, which is modeled by the Discrete Element Method (DEM). Similarly, the theoretical aspects governing DEM and its subsequent coupling to NS equations is introduced, leading to the CFD-DEM framework, a relatively novel approach in granular-fluid modeling. Then, the employed CFD, DEM and CFD-DEM software as well as the simulation setup is rigorously represented to the reader. Subsequently,

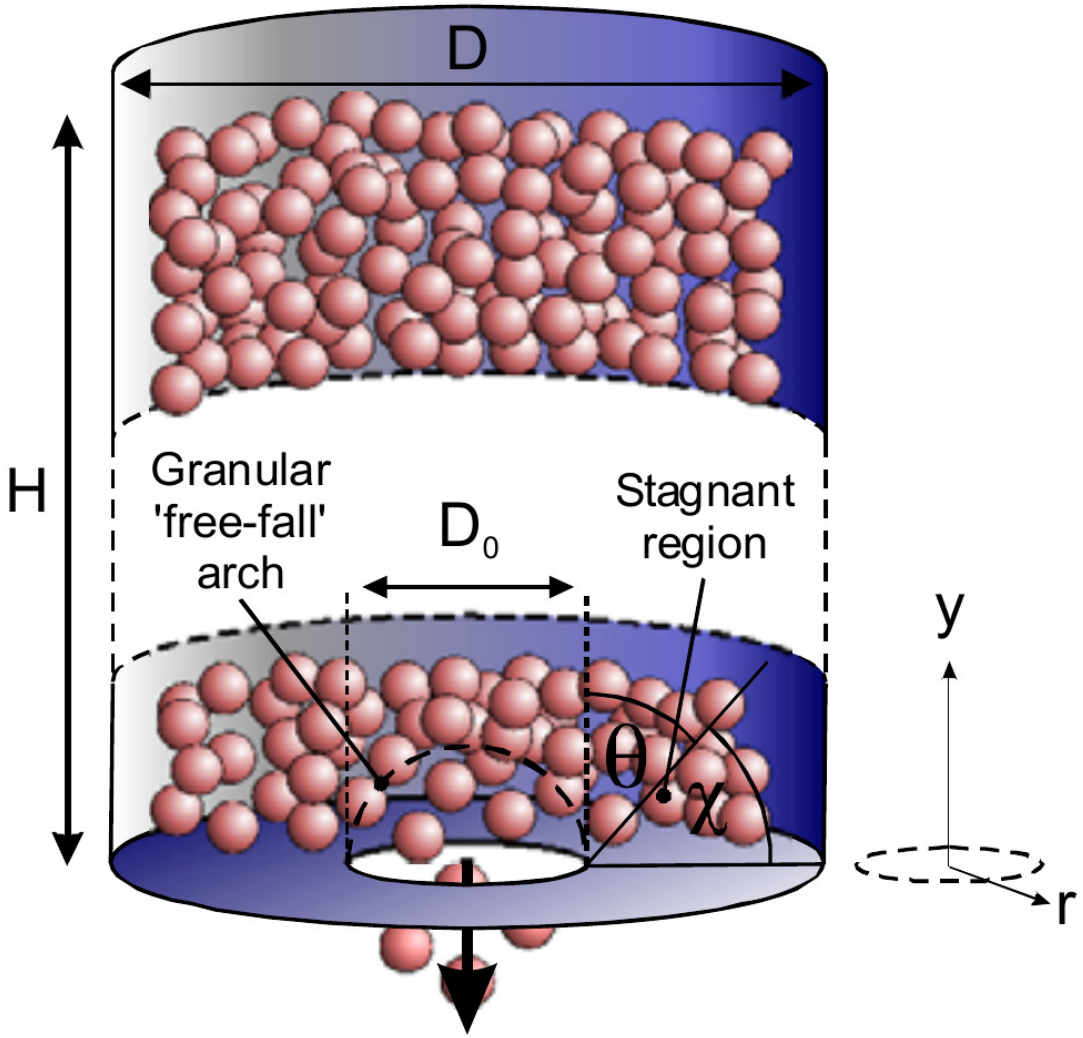

Figure 1: The free-fall arch depicted inside a hopper that is subjected to hopper flow. The arch represents a boundary, above which a single particle remains (on average) stagnant and stuck due to friction imposed by the surrounding particles. Below this boundary, the particles accelerate freely under the gravitational force and exit the hopper. Adopted from Ref. [20].

the relevant results obtained with this CFD-DEM implementation are displayed and compared with experimental data. Finally, the thesis finishes with concluding remarks.

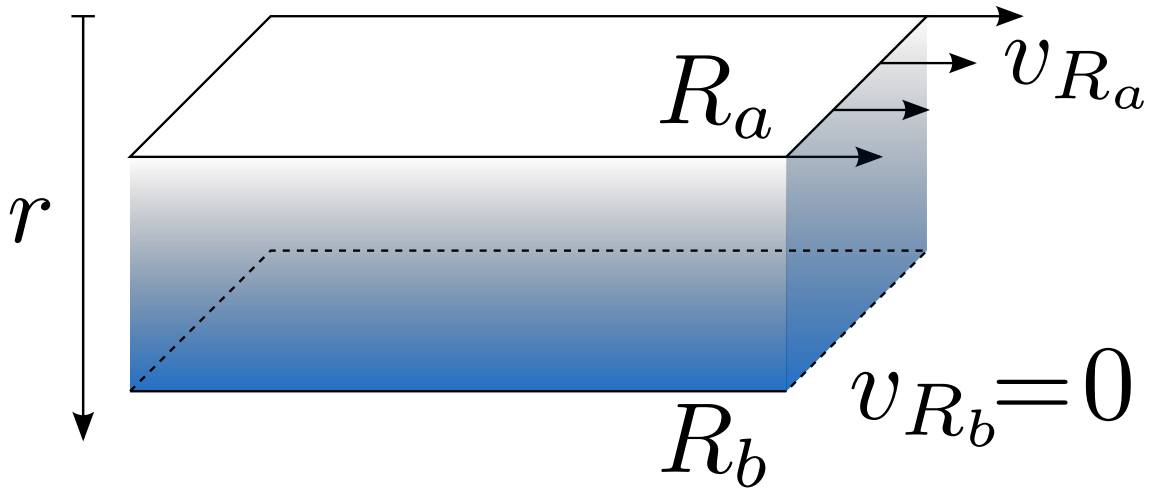

Figure 2: The simple shear flow. Initially, the fluid is confined between two infinitely long plates. Then, the upper plate begins to move, imposing a shear stress σ onto the fluid, forcing it to flow. Assuming no-slip conditions, the fluid sticks to the surfaces completely, and at the upper plate, the fluid velocity corresponds to the velocity of the upper plate (v_{R_a}), while at the lower plate, the fluid remains stationary (v_{R_b}). In a steady-state flow of a Newtonian liquid, the velocity decreases linearly from v_{R_a} to v_{R_b}. Thus, the derivative of the velocity remains constant, and this derivative, designated as the shear rate $\dot{\gamma}$, is defined as $(v_{R_a} - v_{R_b})/L$, where L is the distance between the plates.

2 Theory

As explained earlier, the theoretical approach employed here relies on forming the governing equations for both phases separately at first. However, in order to introduce the reader to the two-phase continuum description of the fluid phase, a necessary prerequisite involves presenting the conservation equations for a (single-phase) fluid. Accordingly, the general balance equation, leading to the renowned Navier-Stokes equations, is first introduced to the reader and the Finite Volume Method (FVM) discretization of these equations is reviewed. Then, proceeding along the course set by the work of Anderson and Jackson [24] and Ishii [25], the idea of local averaging of flow quantities is reviewed, and applied in the subsequent description of the fluid phase in a multi-phase flow. Finally, the DEM methology and its subsequent coupling to the modified Navier-Stokes equations is reviewed.

2.1 Flow quantities

Before advancing onto the fundamental equations of single-phase fluid flow, it is beneficial to introduce the reader to the fundamental flow quantities. The physical meaning of these quantities is best described by a simple example, rather than venturing into a rigorous mathematical description provided by continuum mechanics. Such an example is provided in Fig. 2, which depicts the *simple shear flow*, in which

the fluid is initially confined between two parallel, infinitely long plates. Then, the upper plate begins to move with a fixed velocity (v_{R_a}), and the fluid starts moving as well. This is due to the fact, that the upper plate imposes a *shear stress* σ, *i.e.* a force divided by the cross-section of the plate, on the fluid. Furthermore, if the fluid adheres completely to the plates, the fluid layer at the upper plate (lower plate) has the velocity v_{R_a} (v_{R_b}) as well. For a fluid that is simple enough (Newtonian), the steady-state velocity then decreases linearly in the gap from the value at the upper plate v_{R_a} to that of the lower plate v_{R_b}. Thus, the derivative of the velocity, also called the *shear rate* $\dot{\gamma}$, is constant, and the following equation applies once a steady-state flow is reached [26]

$$\sigma = \eta\dot{\gamma}, \tag{2}$$

where η is the (constant) *viscosity* of the fluid. Eq. (2) provides a useful relationship between the quantities σ, η and $\dot{\gamma}$. For the purposes of this introduction, it can be understood as analogous to an equation of motion for solid objects as it relates the (derivative of) linear velocity to an external force (divided by an area). Following this line of reasoning, one may well conclude that the viscosity η is in fact a quantity, that describes the inherent ability of the fluid to resist flow, as mass describes the intrinsic property of a solid object to resist changes in its motion. However, in practical flow scenarios, the fluid flow is generally more complex than a simple shear flow, and accordingly, instead of scalar quantities, the fundamental flow quantities are described by 3×3 tensors. If we define the x-axis parallel to the plates, and the y-axis perpendicular to these plates in our simple example, the scalar quantities in Eq. (2), would be the second elements in the first row (σ_{xy}, $\dot{\gamma}_{xy}$) of the corresponding tensors $\bar{\bar{\sigma}}$, $\bar{\bar{\dot{\gamma}}}$, since the velocity in the x-direction varies with respect to the spatial y-coordinate. In the following theoretical treatment, the overbars in these tensors are neglected, and the symbols for various flow quantities are assumed tensorial by definition, unless otherwise specified.

2.2 Single-phase flow

An important, yet very intuitive relation describing the conservation of (an abstract) intensive quantity of a fluid reads [25]

$$\frac{d}{dt}\int_{V_m} \rho_k \Phi_k dV = -\oint_{A_m} \mathbf{n_k} \cdot \mathbb{J}_k dA + \int_{V_m} \rho_k \phi_k dV, \tag{3}$$

where V_m and A_m describe the material volume and surface, respectively, k refers to the k^{th} phase, ρ_k is the fluid density, $\mathbf{n_k}$ is the normal vector of the material surface, $\mathbb{J}_k$ is the efflux and ϕ_k is the body source of an intensive quantity Φ_k. In essence, Eq. 3 states that the change of the quantity Φ_k with respect to time is equal to the influx and outflux plus the body source in the control volume. The significance of Eq. 3 will be evident in the following discussion, where it is first converted to a differential form. Then, by introducing appropriate mass quantities Φ_k, it is readily observed that this equation describes the mass and momentum conservation of a single-phase Newtonian fluid. Therefore, it completely describes the behavior of the

fluid in flow. Beginning with the left-hand side of Eq. 3, it would seem feasible to insert the time-derivative inside the volume integral. Since in a flow, the volume element dV might be evolving in time as well, this is best accomplished by applying the renowned Reynolds transport theorem [25]

$$\frac{d}{dt}\int_{V_m}\mathbb{F}_k dV = \int_{V_m}\frac{\partial \mathbb{F}_k}{\partial t}dV + \oint_{A_m}\mathbb{F}_k \mathbf{u_k}\cdot\mathbf{n}dA, \tag{4}$$

where $\mathbf{u_k}$ relates to the velocity of the fluid. Before applying this result to Eq. (3), it is beneficial to transform the latter term in its right-hand side to a volume integral as well. In order to do so, consider first the results of the well-known Gauss's theorem [25, 27]

$$\int_{V_m}\nabla\cdot\mathbb{F}dV = \oint_{A_m}\mathbf{n}\cdot\mathbb{F}dA, \tag{5a}$$

$$\int_{V_m}\nabla f dV = \oint_{A_m}\mathbf{n}f dA, \tag{5b}$$

$$\int_{V_m}\nabla\mathbb{F}dV = \oint_{A_m}\mathbf{n}\mathbb{F}dA. \tag{5c}$$

Now, clearly inserting the result in Eq. 5a to the second right-hand side term of the Reynolds transport theorem provides a useful identity

$$\frac{d}{dt}\int_{V_m}\mathbb{F}_k dV = \int_{V_m}\left(\frac{\partial \mathbb{F}_k}{\partial t} + \nabla\cdot(\mathbf{u}_k\mathbb{F}_k)\right)dV. \tag{6}$$

Eq. 6 can be readily inserted to the left-hand side of Eq. 3. Additionally, the result in Eq. 5a can be applied to the first term on the right-hand side of Eq. 3, which now contains only volume integrals over the same volume element dV. Accordingly, one may dispense with the integration operations, which yields the final (differential) form of the general balance equation [25]

$$\frac{\partial \rho_k\Phi_k}{\partial t} + \nabla\cdot(\mathbf{u_k}\rho_k\Phi_k) = -\nabla\cdot\mathbb{J}_k + \rho_k\phi_k. \tag{7}$$

By fixing the variables appropriately, Eq. 7 can be utilized to depict the conservation of mass, momentum and energy of the fluid. The resulting three equations are usually referred to as the Navier-Stokes equations. However, in this thesis, only the equations governing the mass and momentum conservation are of significant interest, since any temperature induced effects are neglected. Indeed, by setting $\Phi_k = 1$, $\phi_k = 0$ and $\mathbb{J}_k = 0$, Eq. 7 reads [25]

$$\frac{\partial \rho_k}{\partial t} + \nabla\cdot(\rho_k\mathbf{v_k}) = 0. \tag{8}$$

If the Mach-number [28] is small and subsequently, the fluid can be described as incompressible, $\partial\rho_k/\partial t$ is essentially zero, and this reduces to [28]

$$\nabla\cdot\mathbf{u_k} = 0, \tag{9}$$

which is the first Navier-Stokes equation describing the conservation of mass. Furhermore, denoting $\mathbf{g}$ as the gravity acting on the fluid segment and setting $\Phi_k = \mathbf{u_k}$, $\phi_k = \mathbf{g}$ and assuming that the efflux is the result of an external shearing force, expressed conveniently as the Cauchy stress tensor $\mathbb{J}_k = -\mathbb{T}_k$, Eq. 7 yields the second Navier-Stokes equation describing the conservation of momentum [28]

$$\rho_k \cdot \left[\frac{\partial \mathbf{u_k}}{\partial t} + (\mathbf{u_k} \cdot \nabla)\, \mathbf{u_k} \right] = -\nabla \cdot \mathbb{T}_k + \rho_k \mathbf{g_k}, \tag{10}$$

where the stress tensor could be split according to the relation $\mathbb{T}_k = -p_k + \sigma_k$, p denoting the pressure and σ the viscous stress tensor. In fact, this yields a fruitful expression for Eq. 10, since for incompressible Newtonian fluid [28]

$$\nabla \cdot \sigma_k = \nabla \cdot \eta_{fl} \nabla \mathbf{u_k} = \eta_{fl} \nabla \cdot \nabla \mathbf{u_k}, \tag{11}$$

where η_{fl} denotes the (constant) fluid viscosity, the ability of the fluid to resist deformation. Inserting this relation, and the stress tensor in decomposed form to Eq. 10 yields

$$\rho_k \cdot \left[\frac{\partial \mathbf{u_k}}{\partial t} + (\mathbf{u_k} \cdot \nabla)\, \mathbf{u_k} \right] = \nabla p_k - \eta_{fl} \nabla \cdot \nabla \mathbf{u_k} + \rho_k \mathbf{g_k}. \tag{12}$$

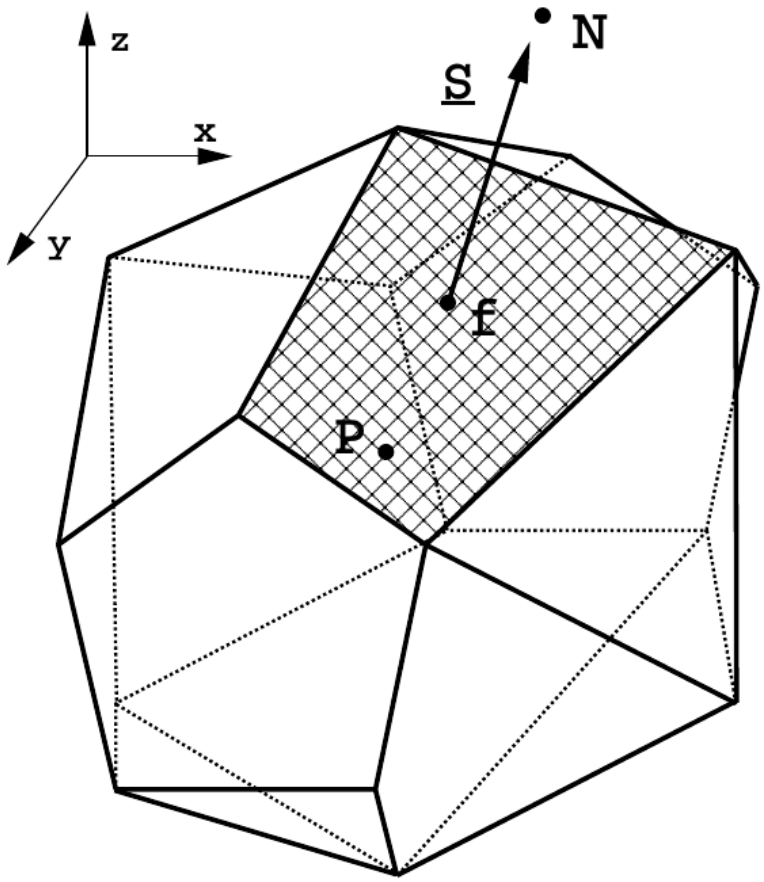

Figure 3: Finite Volume Method: a control volume element (cell) (adapted from Ref. [27]).

2.3 Finite Volume discretization

While Eqs. 10 and 12 seem relatively simple in appearance, no analytic solution exists for them at this time except in certain simplified scenarios. Indeed, verifying or refuting the existence of a general analytic solution to Eq. 12 is considered worth the Millennium prize [29], attesting to the difficulty of the problem. However, various numerical approaches, including the Finite Difference Method, Finite Element Method (FEM) and Finite Volume Method (FVM) [27,30], have proven effective in addressing the problem. Unlike analytic methods, these techniques provide the solution only at certain pre-determined points in space and time. The number and the exact location of these points is determined by the *discretization* process.

The Computational Fluid Dynamics (CFD) framework promoted here makes extensive use of FVM in discretizing and solving Eqs. 9 and 12 and, accordingly, the discretization process is reviewed in the following discussion. In FVM, the computational domain is divided (meshed) into adjacent, non-overlapping control volume elements (cells) displayed in Fig. 3. The data regarding the various flow quantities are stored in the volume centroids of these cells (in Fig. 3, point **p**), yet the

calculations are performed at the cell face centroids (point **f**). The formal definition of the volume centroid, denoted in vector form by $\mathbf{x}_p$, reads [27]

$$\int_{V_p} (\mathbf{x} - \mathbf{x}_p)\, dV = 0, \tag{13}$$

where V_p denotes the finite volume confined in the cell. The face centroid $\mathbf{x}_f$ is expressed as

$$\int_{S_f} (\mathbf{x} - \mathbf{x}_f)\, dS = 0, \tag{14}$$

where S_f denotes the finite area of the face. To preserve computational resources, the required face (centroid) values are generally interpolated from the volume centroid values. Any such interpolation scheme has to provide second-order accuracy, since the second Navier-Stokes equation (Eq. 12) contains second-degree spatial derivatives [27]. As a preliminary development, the Taylor expansion around point **p** provides means to such interpolation, since in the vicinity of $\mathbf{x}_p$ a general scalar quantity ϕ equals to [27]

$$\phi(\mathbf{x}) = \phi_p + (\mathbf{x} - \mathbf{x}_p) \cdot (\nabla\phi)_p \tag{15}$$

with second-degree accuracy. Identically, the second-order expression for a vector quantity **a** reads [27]

$$\mathbf{a}(\mathbf{x}) = \mathbf{a}_p + (\mathbf{x} - \mathbf{x}_p) : (\nabla\mathbf{a})_p, \tag{16}$$

where : denotes the tensorial inner product and the subscript p denotes the ϕ value at $\mathbf{x}_p$. An important property for ϕ follows immediately from the development above [27]

$$\begin{aligned} \int_{V_p} \phi(\mathbf{x}) dV &= \int_{V_p} \left[\phi_p + (\mathbf{x} - \mathbf{x}_p) \cdot (\nabla\phi)_p\right] dV \\ &= \phi_p \int_{V_p} dV + \left[\int_{V_p} (\mathbf{x} - \mathbf{x}_p)\, dV\right] \cdot (\nabla\phi)_p \\ &= \phi_p V_p, \end{aligned} \tag{17}$$

where the second term in the RHS reduces to zero due to the definition of volume centroid given in Eq. 13. Having established these necessary tools for interpolation, the first Navier-Stokes equation (Eq. 9) is then expressed in the integral form and Eq. 5a is applied [27]

$$\int_{V_p} \nabla \cdot \mathbf{u} dV = (\nabla \cdot \mathbf{u})_p V_p = \oint_{S_f} d\mathbf{S} \cdot \mathbf{u} = \sum_f \left(\oint_f d\mathbf{S} \cdot \mathbf{u}\right) = 0, \tag{18}$$

where V_p describes the volume confined in the cell and vector **S** refers to the vector normal to the surface, while the summation $\sum_f$ is over all the confining faces. The remaining integral term in the RHS of Eq. 18 can be further rearranged by inserting the result in Eq. 16 [27]

$$\oint_f d\mathbf{S} \cdot \mathbf{u} = \left(\oint_f d\mathbf{S}\right) \cdot \mathbf{u}_f + \left[\oint_f d\mathbf{S}(\mathbf{x} - \mathbf{x}_f)\right] : (\nabla\mathbf{u})_f = \mathbf{S} \cdot \mathbf{u}_f, \tag{19}$$

where the subscript f denotes the centroid of the face and $\mathbf{u}_f$ and $(\nabla\mathbf{u})_f$ can be moved outside the integrals, since they contain point (constant) values. Additionally, the last term on the RHS in Eq. 19 amounts to zero due to the result in Eq. 14. Now, inserting the expression in Eq. 19 to Eq. 18 yields

$$(\nabla \cdot \mathbf{u})_p V_p = \sum_f \mathbf{S} \cdot \mathbf{u}_f = 0. \tag{20}$$

The result in Eq. 20 states the first conservation law in a very concise way: the flux of $\mathbf{u}$ over all the faces f in the cell has to equal to zero. In fact, this conservation of flow quantities is a very general property of the FVM discretization [27, 30]. Additionally, as seen in Eq. 20, the FVM only operates on surface areas, disregarding the actual shape of the control volume element. Indeed, the FVM can be applied to any geometry provided it can be meshed into a finite amount of conjoined polyhedra [27].

The second Navier-Stokes equation, represented in Eq. 12, can be conveniently expressed in a more simplified form if the fluid density ρ_{fl} is constant, a safe assumption for liquids that are generally incompressible in the experimentally accessible flow scenarios. Thus, for notational brevity, this constant is neglected in the following development, and the equation reads (in integral form) [27]

$$\int_{V_p} \left[\frac{\partial \mathbf{u}}{\partial t} + \nabla \cdot (\mathbf{u}\mathbf{u}) - \nabla \cdot (\eta_{fl} \nabla \mathbf{u}) \right] dV = \int_{V_p} -\nabla p dV, \tag{21}$$

where the spatial derivatives will be discussed first on a cell level. By virtue of Eq. 20, $\int_{V_p} \nabla \cdot (\mathbf{u}\mathbf{u}) dV$ clearly converts to the discretized form [27]

$$\sum_f \mathbf{S} \cdot \mathbf{u}_f \mathbf{u}_f = \sum_f F \mathbf{u}_f, \tag{22}$$

where $F = \mathbf{S} \cdot \mathbf{u}_f$. Regarding Eq. 22, the key issue is to decide on the interpolation scheme for the face centroid values. The most relevant schemes include the central differencing (CD), the upwind differencing (UD) and the blended differencing scheme (BD) [27]. In CD, the value of the face f shared by two neighboring cells, whose volume centroids are denoted by $\mathbf{p}$ and $\mathbf{N}$ is approximated as [27]

$$\mathbf{u}_f = f_x \mathbf{u}_p + (1 - f_x)\, \mathbf{u}_N, \tag{23}$$

where f_x refers to the ratio of the distances [27]

$$f_x = \frac{\overline{fN}}{\overline{pN}}, \tag{24}$$

where $\overline{fN}$ is the separation between the neighboring volume centroid and the face centroid and $\overline{pN}$ is the distance from one volume centroid p to the other N. The CD scheme is second-order accurate [31], but causes unphysical, numerical oscillations when the term $\nabla \cdot (\mathbf{u}\mathbf{u})$ dominates in the second Navier-Stokes equation [32], leading to boundedness of the solution. This can be avoided by the UD scheme, where [27]

$$\mathbf{u}_f = \begin{cases} \mathbf{u}_p & \text{for } F \geq 0 \\ \mathbf{u}_N & \text{for } F < 0, \end{cases} \tag{25}$$

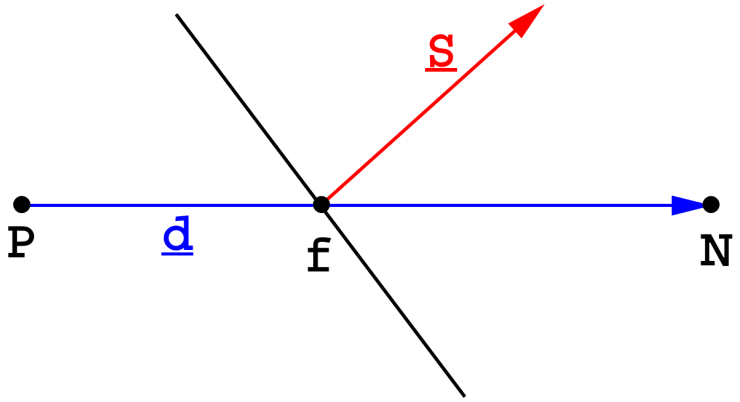

Figure 4: Two neighboring cell volume centroids **p** and **N** are separated by the face f with the normal vector **S**. The relative displacement vector is denoted by **d** (adapted from Ref. [27]).

which ensures the solution is bounded, but invariably results in a loss of accuracy [27].

Applying Eq. 20, the second spatial term in Eq. 21, $\int_{V_p} \nabla \cdot \eta_{fl} \nabla \mathbf{u}_f dV$, converts to

$$\sum_f \mathbf{S} \cdot (\eta_{fl} \nabla \mathbf{u})_f = \eta_{fl} \sum_f \mathbf{S} \cdot (\nabla \mathbf{u})_f \,, \tag{26}$$

where, again, interpolating $(\nabla \mathbf{u})_f$ is the primary concern. Using the CD scheme displayed above, this could be expressed as [27]

$$(\nabla \mathbf{u})_f = f_x (\nabla \mathbf{u})_p + (1 - f_x)(\nabla \mathbf{u})_N, \tag{27}$$

where, deduced identically as the result in Eq. 20, $(\nabla \mathbf{u})_p$ is neatly described by [27]

$$(\nabla \mathbf{u})_p = \frac{1}{V_p} \sum_f \mathbf{S} \mathbf{u}_f. \tag{28}$$

In this context however, the central differencing approach is rarely utilized *per se* due to numerical reasons [27]. Rather, the surface vector **S** is often decomposed to [27]

$$\mathbf{S} = \Upsilon + \mathbf{k}, \tag{29}$$

where Υ is defined parallel to the relative displacement vector **d** between neighboring volume centroids (see Fig. 4). Consequently, the dot product in Eq. 26 can be rewritten as

$$\mathbf{S} \cdot (\nabla \mathbf{u})_f = \underbrace{\Upsilon \cdot (\nabla \mathbf{u})_f}_{\text{orthogonal contr.}} + \underbrace{\mathbf{k} \cdot (\nabla \mathbf{u})_f}_{\text{non-orthogonal contr.}} \,, \tag{30}$$

where the orthogonal term can be calculated simply as

$$\Upsilon \cdot (\nabla \mathbf{u})_f = |\Upsilon| \frac{\mathbf{u}_N - \mathbf{u}_p}{|\mathbf{d}|}, \tag{31}$$

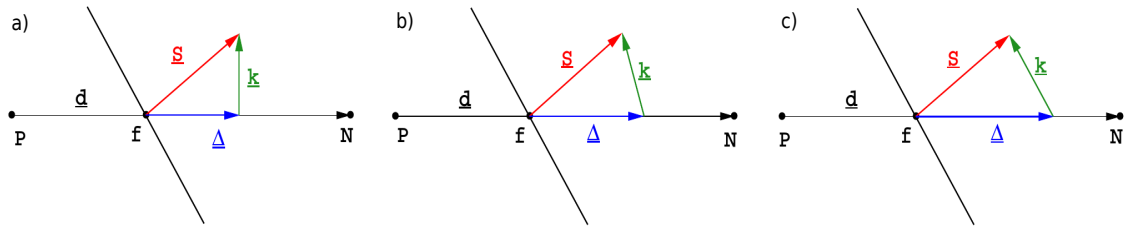

Figure 5: a) the minimum correction approach (MCA), b) the orthogonal correction approach (OCA) and c) the over-relaxed approach (ORA) to decomposing $\mathbf{S}$ (adapted from Ref. [27]).

and the CD scheme, as represented in Eq. 27, is applied to the non-orthogonal term in Eq. 30. The techniques for calculating Υ include the minimum correction approach (MCA), the orthogonal correction approach (OCA) and the over-relaxed approach (ORA) [27]. In MCA (see Fig. 5a)), Υ and $\mathbf{k}$ are orthogonal, and Υ equals to [27]

$$\Upsilon = \frac{\mathbf{d} \cdot \mathbf{S}}{\mathbf{d} \cdot \mathbf{d}} \mathbf{d}, \tag{32}$$

which ensures that Υ is parallel to $\mathbf{d}$. Then, $\mathbf{k}$ is defined from Eq. 29. In OCA (see Fig. 5b)), Υ reads [27]

$$\Upsilon = \frac{|\mathbf{S}|}{|\mathbf{d}|} \mathbf{d}, \tag{33}$$

and $\mathbf{k}$ is calculated from Eq. 29. Finally, in ORA (see Fig. 5c)), Υ amounts to [27]

$$\Upsilon = \frac{|\mathbf{S}|^2}{\mathbf{d} \cdot \mathbf{S}} \mathbf{d}, \tag{34}$$

while $\mathbf{k}$ is again provided by Eq. 29. Subsequently, the second spatial derivative term in Eq. 21 can be discretized to yield [27]

$$\eta_{fl} \sum_f \mathbf{S} \cdot (\nabla \mathbf{u})_f = \eta_{fl} \sum_f |\Upsilon| \frac{\mathbf{u}_N - \mathbf{u}_p}{|\mathbf{d}|} + \mathbf{k} \cdot (\nabla \mathbf{u})_f. \tag{35}$$

The discretization of the final spatial derivative, ∇p, is omitted at this point and discussed later in conjunction with the PISO-algorithm. Thus, only the temporal discretization of $\partial/\partial t \int_{V_p} \mathbf{u} dV$ in Eq. 21 remains unaddressed. The most renowned schemes to this end include the second-order Crank-Nicholson discretization, the first-order explicit discretisation and the first-order implicit Euler method [27]. In this thesis, only the implicit Euler scheme is utilized. As the cells composing the mesh are invariant with respect to time, the volume elements in Eq. 21 are unaffected. Additionally, applying the result in Eq. 17, the momentum equation is expressed with the implicit Euler method as [27]

$$\frac{\mathbf{u}_p^n - \mathbf{u}_p^0}{\Delta t} V_p + \sum_f F \mathbf{u}_f^n - \eta_{fl} \sum_f \mathbf{S} \cdot (\nabla \mathbf{u})_f^n = -\nabla p^n V_p, \tag{36}$$

where the superscripts n and 0 refer to the value of the new and old time-step, respectively. Now, inserting the results from Eqs. 23, 27 and 35 to Eq. 36 and dividing by V_p clearly provides the second Navier-Stokes equation in a discretized form, where the only unknown variables are $\mathbf{u}_p^n$ and $\mathbf{u}_N^n$ and the pressure term $-\nabla p$. Indeed, this reads [27]

$$\alpha_p \mathbf{u}_p^n = \mathbf{H} - \nabla p = -\sum_N \alpha_N \mathbf{u}_N^n + \frac{\mathbf{U}_0}{\Delta t} - \nabla p, \tag{37}$$

where the coefficients α_p and α_N contain the known factors, such as old time-step data, resulting from the discretization process. As Eq. 37 can be formulated for each cell, this results in a linear system of equations of the form [27]

$$[A]\,[\mathbf{u}] = [R]\,, \tag{38}$$

where $[R]$ contains the RHS terms of Eq. 37 and the added boundary conditions regarding $\mathbf{u}$ ensure that the amount of equations matches the number of unknown cell velocities, and subsequently, a unique solution. In theory, this set of equations can be then calculated using either direct or iterative linear solvers [27], although the iterative methods are more popular for large system sizes [27], for which direct solvers are computationally more expensive.

However, for each cell, the pressure term $-\nabla p$ residing in the RHS of Eq. 37 imposes a profound impediment on the possible overall solution, since on a general level, no constitutive relationship between p and $\mathbf{u}$ exist. Due to this reason, a variety of velocity-pressure coupling algorithms have been developed, generally classified to simultaneous or segregated approaches [27]. In this work, the Pressure Implicit with Splitting of Operator (PISO) algorithm first introduced by Issa [33] is applied to provide such (segregated) coupling. Accordingly, the result in Eq. 37 is first rearranged to yield [27]

$$\mathbf{u}_p^n = \frac{\mathbf{H}}{\alpha_p} - \frac{1}{\alpha_p}\nabla p, \tag{39}$$

which when interpolated to a face centroid, is trivially expressed as [27]

$$\mathbf{u}_f = \left(\frac{\mathbf{H}}{\alpha_p}\right)_f - \left(\frac{1}{\alpha_p}\right)_f (\nabla p)_f\,. \tag{40}$$

Now, inserting this result to Eq. 20 and operating by $\nabla\cdot$ on both sides yields [27]

$$\nabla\cdot\left(\frac{1}{\alpha_p}\nabla p\right) = \sum_f \mathbf{S}\cdot\left[\left(\frac{1}{\alpha_p}\right)(\nabla p)_f\right] = \nabla\cdot\left(\frac{\mathbf{H}}{\alpha_p}\right) = \sum_f \mathbf{S}\cdot\left(\frac{\mathbf{H}}{\alpha_p}\right)_f, \tag{41}$$

which, in the context of the PISO algorithm, is referred to as the pressure equation. The PISO algorithm then operates in the following manner [27]

1. The discretized momentum equation, depicted in Eq. 37 is solved first. The unknown pressure gradient term is neglected, and the known pressure value from the old time-step is used instead. The intermediate velocity field is thus obtained.

2. Using the intermediate velocity field, the **H** operator is constructed, allowing the pressure to be solved from the pressure equation (Eq. 41).

3. The new pressure value is then inserted to Eq. 39 and a new value for the velocity field is obtained. Again, this can be used to evaluate **H**, which in turn is applied in the pressure equation to provide yet another (corrected) value for the pressure. The cycle is continued for prescribed number of times until a pre-determined error tolerance is reached.

2.4 Local averaging

It is clear that together, Eqs. 9 and 10 provide a powerful tool for evaluating, for instance, the fluid velocity field once the appropriate constitutive relations for other quantities, such as stress, are established. However, introducing similar continuum descriptions for each phase in a multi-phase mixture poses formidable mathematical problems. As these phases form interfaces between each other, these interfaces might move and deform in unknown ways, complicating the mathematical description considerably. Additionally, the continuum description as such is not applicable at the (possibly) significant discontinuities imposed by these interfaces [25]. Moreover, the possible interactions, such as mass or momentum transfer across these interfaces have to be accounted for [25]. Consequently, in order to recover the continuum picture of the flow dynamics, appropriate averaging of local flow variables of each phase has to be performed. This then results in Eqs. 9 and 10 being expressed in terms of average flow quantities. Essentially, this approach leads to describing the phases as interpenetrating continuum media [23, 24]. The subsequent discussion follows the work of Anderson and Jackson [24], where the two phases consisted of solid particles embedded in an interstitial fluid. However, as the present work utilizes a more recent method (DEM) in modeling the solid particles, the continuum description of the solid phase is ignored.

The spatial averaging procedure (as described in Ref. [24]) for the flow quantities necessitates a "weighing" function. Let $g(r)$ be such a function, defined for all $r \in (0, \infty)$. Here, r refers to the distance from a point in three-dimensional space and V_∞ denotes the volume over the whole of this space. Furthermore, g has the following properties [24]

- g decreases monotonically as r increases,
- g possesses derivatives $g^{(n)}(r)$ for all orders and for each value of r,
- $\int_{V_\infty} g^{(n)}(r)$ exists for all r and
- $\int_{V_\infty} g(r)dV = 4\pi \int_0^\infty g(r)dr = 1$.

At this point, the exact definition of g is not important. However, the radius r_0 associated with g is defined so that

$$4\pi \int_0^{r_0} g(r)r^2 dr = 4\pi \int_{r_0}^{\infty} g(r)r^2 dr = \frac{1}{2}. \tag{42}$$

Indeed, as discussed later, if this radius meets certain conditions, the exact formulation of g is irrelevant.

The guiding principle is to recast Eqs. 9 and 10 by integrating each term (weighed by g) in the original equations over the volume occupied by the fluid. The subsequent integrodifferential equations are then systematically examined and modified term by term to yield a description consisting exclusively of differential operators as in the original NSEs, yielding the two-phase description of the fluid. For the sake of brevity, the rigorous derivation of these two-phase Navier-Stokes equations complete

with the commentary on their range of applicability, is performed in Appx. A. The final results read

$$\frac{\partial \epsilon_{fl}}{\partial t} + \nabla \cdot (\epsilon_{fl}\mathbf{u}) = 0 \tag{43}$$

and

$$\rho_{fl}\epsilon_{fl}\left[\frac{\partial \mathbf{u}}{\partial t} + \nabla \cdot (\mathbf{uu})\right] = \nabla \cdot \mathbb{T}_k - n\mathbf{f} + \rho_{fl}\epsilon_{fl}\mathbf{g}, \tag{44}$$

where ϵ_{fl} describes the volume fraction occupied by the fluid, n is the number of particles in the control volume element and $\mathbf{f}$ is the particle-fluid interaction term, that explicitly describes the various interactions between the two phases. This term is detailed later in Sec. 2.5.

The result displayed in Eq. 44, supplemented with the laminar flow assumption, is generally referred to as 'set I' in the literature governing CFD-DEM modeling [23]. It should be noted, that the discretization procedure for a single phase fluid described in Sec. 2.3 is completely applicable for this equation as well with the additional assumption: the term $\mathbf{f}$ is calculated as the average force $(1/N) \cdot \sum_i^N f_i$, where the summation is over the particles located in a cell. The accompanying continuum equation for the solid phase (though not derived here) reads [23]

$$\rho_s\epsilon_s\left[\frac{\partial \mathbf{v}}{\partial t} + \nabla \cdot (\mathbf{vv})\right] = n\Phi - \nabla \cdot \mathbf{S} + \mathbf{f} + \rho_s\epsilon_s\mathbf{g}, \tag{45}$$

where ρ_s is the density of the solid phase, ϵ_s $(= 1 - \epsilon_{fl})$ is the solid volume fraction, $\mathbf{v}$ is the solid velocity, Φ is the local mean value of particle-particle interaction force and $\mathbb{S}_k$ is a tensor representing 'Reynold stresses'. However, approximating the undetermined constitutive relationships for quantities (such as $\mathbf{f}$ or $-\nabla \cdot \mathbb{S}_k$) results in a slightly altered form for these conservation equations. Indeed, in the same vein as in Appx. A, the fluid-particle interaction term $n\mathbf{f}$ can be decomposed into two terms: one corresponding the 'macroscopic', and the other the local fluctuations with scale on par with particle spacings [23]

$$n\mathbf{f} = n\frac{V_p \nabla \cdot \mathbb{T}_k}{\Delta V} + n\mathbf{f}' = \epsilon_s \nabla \cdot \mathbb{T}_k + n\mathbf{f}', \tag{46}$$

where the first term on the right-hand side denotes the fluid-particle interactions due to 'macroscopic' variations and the second term due to local fluctuations. Furthermore, a constitutive relation for the solid stress tensor $\mathbb{T}_k^s$ of the form [23]

$$-\nabla \cdot \mathbb{T}_k^s = n\Phi - \nabla \cdot \mathbb{S}_k \tag{47}$$

together with Eq. 46 now allow Eqs. 44 and 45 to be formulated as [23]

$$\rho_{fl}\epsilon_{fl}\left[\frac{\partial \mathbf{u}}{\partial t} + \nabla \cdot (\mathbf{uu})\right] = \epsilon_{fl}\nabla \cdot \mathbb{T}_k - n\mathbf{f}' + \rho_{fl}\epsilon_{fl}\mathbf{g} \tag{48a}$$

$$\rho_s\epsilon_s\left[\frac{\partial \mathbf{v}}{\partial t} + \nabla \cdot (\mathbf{vv})\right] = \epsilon_s\nabla \cdot \mathbb{T}_k + n\mathbf{f}' + \rho_s\epsilon_s\mathbf{g} + \nabla \cdot \mathbb{T}_k^s, \tag{48b}$$

acknowledged as 'set II' in the literature [23]. Now, multiplying Eq. 48a by $(1-\epsilon_{fl})/\epsilon_{fl}$ and subtracting Eq. 48b from the result yields

$$\rho_s\epsilon_s\left[\frac{\partial \mathbf{v}}{\partial t}+\nabla\cdot(\mathbf{vv})\right]=n\frac{\mathbf{f}'}{\epsilon_{fl}}-\rho_{fl}\epsilon_s\mathbf{g}+\rho_{fl}\epsilon_s\left[\frac{\partial \mathbf{u}}{\partial t}+\nabla\cdot(\mathbf{uu})\right]+\rho_s\epsilon_s\mathbf{g}+\nabla\cdot\mathbb{T}_k^s, \quad (49)$$

which is yet another representation for the solid phase. Here, the fluid stress tensor $\mathbb{T}_k$ has vanished and replaced with a buoyancy term $-\rho_{fl}\epsilon_s\mathbf{g}$ and the term $\rho_{fl}\epsilon_s\left[\partial\mathbf{u}/\partial t+\nabla\cdot(\mathbf{uu})\right]$, which describes the fluid acceleration in the particle frame of reference. If this term approaches zero, *i.e.* the fluid flow is steady and uniform, or is significantly smaller than $n\mathbf{f}'/\epsilon_{fl}-\rho_{fl}\epsilon_s\mathbf{g}$, the total particle-fluid interaction force on the particles amounts to [23]

$$n\mathbf{f}=n\frac{\mathbf{f}'}{\epsilon_{fl}}-\rho_{fl}\epsilon_s\mathbf{g}, \quad (50)$$

which, when incorporated to Eqs. 44 and 45 together with the assumption given in Eq. 47, results in the final set of conservation equations, known as 'set III' [23]

$$\rho_{fl}\epsilon_{fl}\left[\frac{\partial \mathbf{u}}{\partial t}+\nabla\cdot(\mathbf{uu})\right]=\nabla\cdot\mathbb{T}_k-\left(n\frac{\mathbf{f}'}{\epsilon_{fl}}-\rho_{fl}\epsilon_s\mathbf{g}\right)+\rho_{fl}\epsilon_{fl}\mathbf{g} \quad (51a)$$

$$\rho_s\epsilon_s\left[\frac{\partial \mathbf{v}}{\partial t}+\nabla\cdot(\mathbf{vv})\right]=\nabla\cdot\mathbb{T}_k^s+\left(n\frac{\mathbf{f}'}{\epsilon_{fl}}-\rho_{fl}\epsilon_s\mathbf{g}\right)+\rho_s\epsilon_s\mathbf{g}, \quad (51b)$$

which, as stated above, is only valid when the fluid flow is steady, uniform and non-accelerating.

Sets I (Eq. 44), II (Eq. 48a) and III ((Eq. 51a)) provide three distinct approaches to modeling fluid-solid flows. However, since sets II and III contain continuum assumptions regarding the constitutive relations for both $\mathbb{T}_k^s$ and $n\mathbf{f}$, they are expected to be non-applicable in the present work, where the solid (granular) phase is modeled as a discrete phase. Furthermore, in this work, the forces acting on an individual particle and a control volume fluid element can be calculated directly (as seen later Sec. 2.5), and approximations relating to $n\mathbf{f}$ are considered unnecessary. It is due to these arguments that 'set I' is used throughout this work, containing the minimal amount of additional assumptions regarding the flow.

Finally, it should be noted that the FVM-discretization is applicable to these sets in the same manner as explained in Sec. 2.3 for the single-phase NS equations, albeit the rigorous derivation is more tedious. In particular, the discretization results in formally identical linear equations as the one displayed in Eq. 37, which is complemented with the averaged fluid-particle interaction term. As such, they are composed of the coefficients α_p, α_N, the operator $\mathbf{H}$, the pressure term and $\mathbf{f}$. Thus, these equations are assembled into a linear system and the PISO-algorithm can be applied normally.

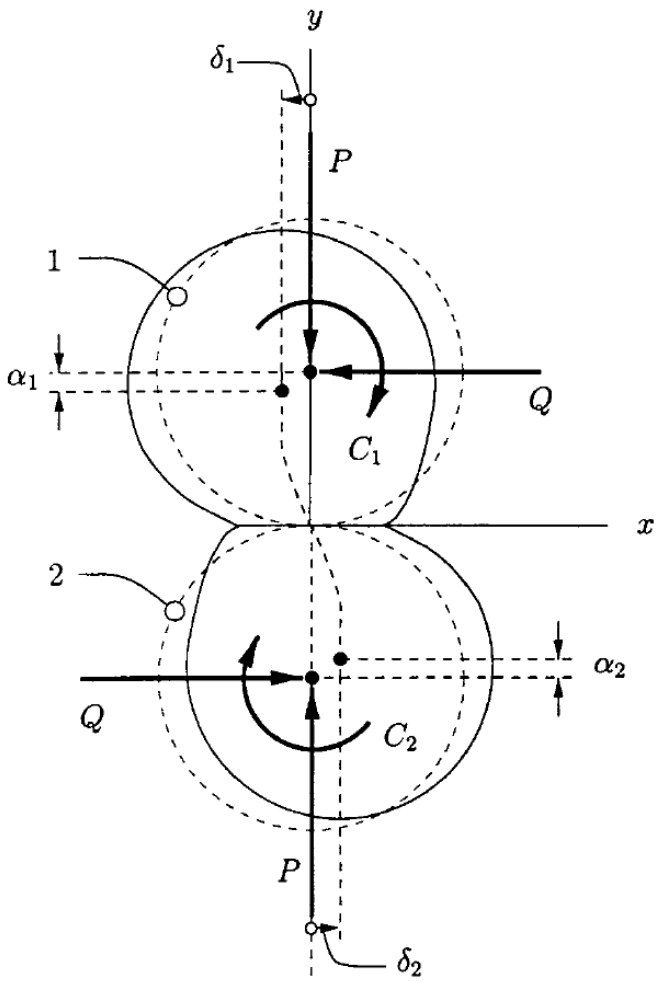

Figure 6: DEM: two particles interacting via a collision (adapted from [22]). The particles are allowed to overlap slightly, although the magnitude of this overlap is modest in comparison to particle radii [34]. The overlap (*e.g.* for particle 1) can be divided to normal (α_1) and tangential components (δ_1).

2.5 Discrete Element Method (DEM)

The Discrete Element Method (DEM), first introduced by Cundall and Strack [22], is a numerical approach belonging to the class of soft-sphere models [35, 36]. In these models, each particle forming the solid phase is tracked individually and its movement defined by Newton's second law [22]. The particles may also interact by collisions or short-range forces, such as van der Waals forces [21]. Other underlying assumptions embedded in the method are

- the chosen time-step Δt of the system is constant,
- while interacting (such as colliding), the velocity and acceleration of an individual particle remain constant for the duration of a time-step,

- particles are allowed to overlap slightly while colliding (see Fig. 6),
- the designated time-step is small enough, so that the "disturbances" or interactions caused by a single particle are experienced only by the particles in its immediate surroundings.

In the context of this work, short-range forces, such as van der Waals interactions, are ignored, and the subsequent presentation assumes any external forces acting on an individual particle are due to particle-fluid interactions, particle-particle collisions, gravity and a contact damping force [22, 23]. More specifically, the approach in DEM is to determine the Newton's second law for each particle [23]

$$m_i \frac{d\mathbf{v}_i}{dt} = \mathbf{f}_{pf,i} + \sum_{j=1}^{k_c} \left(\mathbf{f}_{c,ij} + \mathbf{f}_{da,ij}\right) + m_i \mathbf{g} \tag{52a}$$

$$I_i \frac{d\omega_i}{dt} = \sum_{j=1}^{k_c} \left(\mathbf{M}_{t,ij} + \mathbf{M}_{r,ij}\right), \tag{52b}$$

where m_i is the mass of an individual particle, $\mathbf{v}_i$ is the vector denoting its velocity, $\mathbf{f}_{pf,i}$ is the particle-fluid interaction force (identical to $\mathbf{f}_i$ in Eq. 44), k_c denotes the number of the neighbouring (interacting) particles, $\mathbf{f_{c,ij}}$ is the elastic force term resulting from the overlap of the particle with the neighbouring particles, $\mathbf{f}_{da,ij}$ is the viscous damping force, and $\mathbf{g}$ denotes the gravity vector. Furthermore, I_i refers to the moment of inertia of the particle and ω_i the angular velocity of the particle. Both $\mathbf{M}_{t,ij}$ and $\mathbf{M}_{r,ij}$ arise from the particle-particle interactions as well, refering to the torque generated by the tangential force and 'rolling friction', respectively. Once the constituents in Eq. 52a are known, the new velocity and position of the particle is determined by simple Verlet integration [37].

The force terms in Eq. 52a require further elaboration. The particle-fluid interaction force $\mathbf{f}_{pf,i}$ is the sum of multiple interaction terms, whose degree of contribution to the total interaction force may vary significantly depending on the flow scenario. The terms include [23]

$$\mathbf{f}_{pf,i} = \mathbf{f}_{d,i} + \mathbf{f}_{\nabla p,i} + \mathbf{f}_{\nabla \cdot \mathbb{T}_k,i} + \mathbf{f}_{vm,i} + \mathbf{f}_{B,i} + \mathbf{f}_{Saff,i} + \mathbf{f}_{Mag,i}, \tag{53}$$

where the various force terms are described in Tab. 1. It should be noted, however, that generally for all these terms, the mathematical correlations are widely contested, and multiple definitions exist in the literature. Especially in the case of the drag force $\mathbf{f}_d$, the theory is well established for a single, isolated particle in various flow schemes, but the presence of neighbouring particles complicates the situation considerably [21], being no doubt the primary reason for the vast range of drag models that have been proposed over time. Indeed, the drag force $\mathbf{f}_d$ has been under considerable scrutiny, and various theoretical or empirical correlations, including those suggested by Ergun [43], Wen and Yu [44], Di Felice [45] and Koch and Hill [46] have been suggested. To avoid encumbering the presentation, these models are examined in more detail in Appx. B.

Table 1: The various force terms in Eq. 53 explained.

Force	Origin	References
$\mathbf{f}_{d,i}$, drag force	interstitial fluid phase resists/forces the movement of the solid phase (see below)	[21]
$\mathbf{f}_{\nabla p}$, pressure gradient force	pressure difference across the particle surface (incl. buoyancy)	[21, 24]
$\mathbf{f}_{\nabla\cdot\mathbb{T}_k}$, shear stress force	fluid shear stress imposes a net force on an embedded particle	[38]
$\mathbf{f}_{vm}$, virtual mass force	the surrounding fluid induces additional resistance for an accelerating particle	[21, 39]
$\mathbf{f}_B$, Basset force	the lagged build-up of the fluid boundary layer around a particle in unsteady flow introduces an additional drag force	[21, 40]
$\mathbf{f}_{Saff}$, Saffman force	lift force due fluid inertia effects around the particle	[21, 41]
$\mathbf{f}_{Mag}$, Magnus force	lift force due to interplay of particle rotational velocity and the velocity of the surrounding fluid	[21, 42]

The second term in Eq. 52a, the elastic force $\mathbf{f}_c$, results from the overlap between colliding particles, as these particles resist deformation. Fig. 6 illustrates this overlap δ, which can be decomposed to normal displacement δ_n and tangential displacement δ_t. Correspondingly, the elastic force itself can be expressed component-wise $\mathbf{f}_{c,n}$ and $\mathbf{f}_{c,t}$, denoting the normal and tangential directions, respectively. The relation between the force and the corresponding deformation is not trivial to establish, since this can be affected, for instance, by particle shape, state of movement and material properties [21]. The two models examined here include the linear spring-dashpot model by Cundall and Strack [22] and the more complicated, non-linear Hertz-Mindlin and Deresiewicz model [21]. In the linear spring-dashpot model, the displacements relate to the forces as [22]

$$\mathbf{f}_{c,n} = -K_n \delta_n \mathbf{n}_c, \tag{54a}$$

$$\mathbf{f}_{c,t} = -K_t \mathbf{v}_c^t, \tag{54b}$$

where K_n and K_t denote the normal and shear stiffnesses, respectively, and $\mathbf{n}_c$ is the relative displacement vector between the interacting particles. Additionally, $\mathbf{v}_c^t$ refers to the tangential component of the relative velocity vector between the particles. In essence, Eqs. 54a and 54b treat the colliding particles as Hookean springs, which is applicable if the particle deformations are small and the particles can be considered hard spheres. However, a more sophisticated (and complete) model suggesting non-linearity of these interactions was first presented in the normal direction by Hertz [47] and complemented later in the tangential direction by Mindlin and Deresiewicz [48].

The equations read [21, 23, 49, 50]

$$\mathbf{f}_{c,n} = -\frac{4}{3}E^*\sqrt{R^*}\delta_n^{3/2}\mathbf{n}_c, \tag{55a}$$

$$\mathbf{f}_{c,t} = -\mu_s|\mathbf{f}_{c,n}|\left[1-\left(1-\frac{\delta_t}{\delta_{t,max}}\right)^{3/2}\right]\hat{\mathbf{v}}_c^t, \tag{55b}$$

where E^* and R^* denote the 'equivalent' Young's modulus and radius, respectively, and μ_s is the effective friction coefficient of the two particles. Additionally, $\delta_{t,max}$ represents the maximum value, at which the Coulomb friction law holds. Any tangential overlap exceeding this value no longer contributes to the tangential contact force, since the particles are effectively slipping past each other.

The third term in Eq. 52a refers to the contact 'damping' forces [22], that could be best characterized as a loss term, describing the energy-dispersing nature of the granular system. Since the contact damping forces are specific to the contact model at hand, they are frequently included in the elastic force term. Indeed, for the linear spring-dashpot model, the contact (viscous) damping terms are [21, 23]

$$\mathbf{f}_{da,n} = -C_n\left(\mathbf{v}_c\cdot\mathbf{n}_c\right)\mathbf{n}_c \tag{56a}$$

$$\mathbf{f}_{da,t} = C_t\left(\mathbf{v}_c\times\mathbf{n}_c\right)\times\mathbf{n}_c, \tag{56b}$$

where C_n and C_t are the damping constants. For the non-linear Hertz-Mindlin and Deresiewicz theory, the viscous damping terms equal to [21, 23]

$$\mathbf{f}_{da,n} = -C_n\left(8m_{ij}E^*\sqrt{R^*\delta_n}\right)^{1/2}\cdot\left(\mathbf{v}_c\cdot\mathbf{n}_c\right)\mathbf{n}_c, \tag{57a}$$

$$\mathbf{f}_{da,t} = -C_t\left(6\mu_s m_{ij}|\mathbf{f}_{c,n}|\sqrt{1-\frac{|\delta_t|}{\delta_{t,max}}}/\delta_{t,max}\right)^{1/2}\cdot\left(\mathbf{v}_c\times\mathbf{n}_c\right)\times\mathbf{n}_c, \tag{57b}$$

where $m_{ij} = 1/m_i + 1/m_j$. Although the exact form of the damping constants C_n and C_t varies between the contact models, they both invariably depend on the interparticle coefficient of restitution e. This parameter describes the degree of energy loss in the particle-particle collisions.

To conclude this section, the torque by tangential forces $\mathbf{M}_t$ and rolling friction $\mathbf{M}_r$ in Eq. 52b are briefly discussed. The former of these two can be written simply as [23]

$$\mathbf{M}_{t,ij} = \mathbf{R}_{ij}\times\left(\mathbf{f}_{c,n,ij}+\mathbf{f}_{da,n,ij}\right), \tag{58}$$

whereas the latter requires further elaboration. The relative rotation of interacting particles produces a rolling resistance at the contact area, and the associated torque can be expressed as [51]

$$\mathbf{M}_{r,ij} = -\mu_r\mathbf{f}_{c,n,ij}\hat{\omega}_i, \text{or} \tag{59a}$$

$$\mathbf{M}_{r,ij} = -\mu_r\Psi_{\omega,ij}\mathbf{f}_{c,n,ij}\hat{\omega}_i, \tag{59b}$$

where μ_r is the rolling friction coefficient and Ψ denotes the relative tangential velocity of the particles at the contact surface. The latter expression, derived by Brilliantov *et al.* [52], is slightly different from Eq. 59a, as the torque is also dependent on the relative tangential velocity.

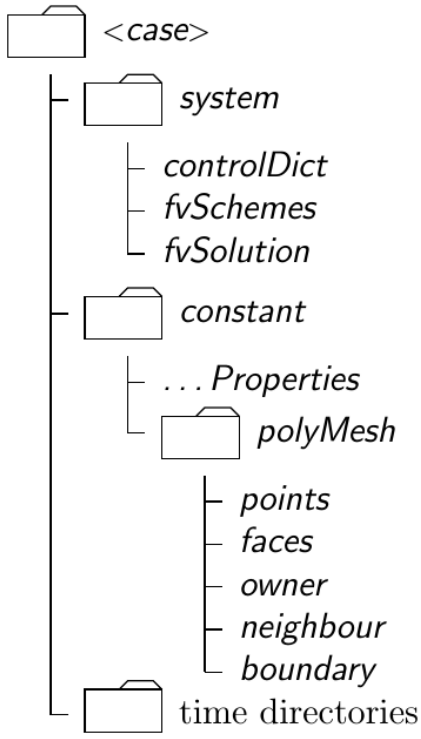

Figure 7: OpenFOAM: the standard case structure (adapted from Ref. [53]).

3 Implementation

3.1 OpenFOAM®

OpenFOAM® [53] is an open-source Computational Fluid Dynamics (CFD) library written in C++ that provides tools for meshing and a collection of solvers for both compressible and incompressible fluid flow complete with extensive post-processing features. The various solvers pertaining, for instance, to turbulent and laminar monophase flow have been validated quite extensively [54, 55] and the suite is also capable of parallel execution, generally exhibiting reasonable scaling properties [56,57].

On a general level, the specific flow scenario and its solution are stored in a 'case' folder displayed in Fig. 7. As a minimum setup, this case file contains the 'system', 'constant' and a number of 'time' folders designated by simulation time. The system folder includes a collection of files that contain parameters associated with the solution itself. These include, for instance, the time-step chosen for integration, the discretization schemes for the Navier-Stokes equations and the the list of solvers used in resolving these discretized linear equations. The constant folder includes the various constants associated with the equations (*e.g.* the value of viscosity) as well as the meshed flow geometry ('polyMesh' directory). Finally, the time folders are created in designated intervals controlled by the user, and they contain the solutions for each flow quantity (*e.g.* fluid velocity) over the whole simulation domain at the time specified by the folder name. As a prerequisite, the user must supply a folder

labeled '0' and provide the initial values as well as the boundary conditions for each quantity, and the rest are computed by the program during run-time.

Regarding user interface, the library has no GUI or central management system. Rather, the user provides calls to various functions and sub-routines directly from the command-line. While the standard distributions have heavily favored Debian-based Linux operating systems, a Windows-compliant version has also been recently released.

3.2 LIGGGHTS®

An open-source DEM simulation software written in C++, LIGGGHTS® [58] is built upon the foundation laid out by LAMMPS [59], an open-source Molecular Dynamics (MD) simulation software developed and maintained by Sandia National Laboratories. Designed as an improvement to LAMMPS to better address granular systems, LIGGGHTS sports full DEM capabilities as outlined in Sec. 2.5 and includes numerous additional features, such as heat conduction for contacting particles. At present, the code is parallelized using the Message Passing Interface (MPI), although advanced designs have been recently devised to improve scaling [60].

The simulations are run from the command-line interpreter by providing the LIGGGHTS binary executable with the appropriate input scripts. These scripts, written in LIGGGHTS pseudocode, define at least the following:

- the simulation domain and the applied geometry (either constructed from primitives or imported CAD design), as well as its parallelization,
- (particle) material properties as well as size (distribution),
- particle insertion to the applied geometry,
- integration scheme and time-step,
- particle-particle and particle-wall contact models,
- data outputted by the program.

At present, LIGGGHTS is supported and regularly updated by the CFDEM®project team. The officially supported platforms include Debian-based Linux distributions, including the prominent Ubuntu operating system.

3.3 The CFDEM®project

The CFDEM®project is an open-source interface that combines OpenFOAM [53] with LIGGGHTS® [58]. It allows the user a great degree of control over the coupled simulation, having the volume-averaged Navier-Stokes sets I, II and III (see Sec.2.4) readily implemented in the software. Additionally, the various particle-fluid interaction terms and drag models reviewed in Sec. 2.5 can also be enabled at will. At this time, the software still lacks a sophisticated GUI, and is operated entirely via user-supplied input scripts.

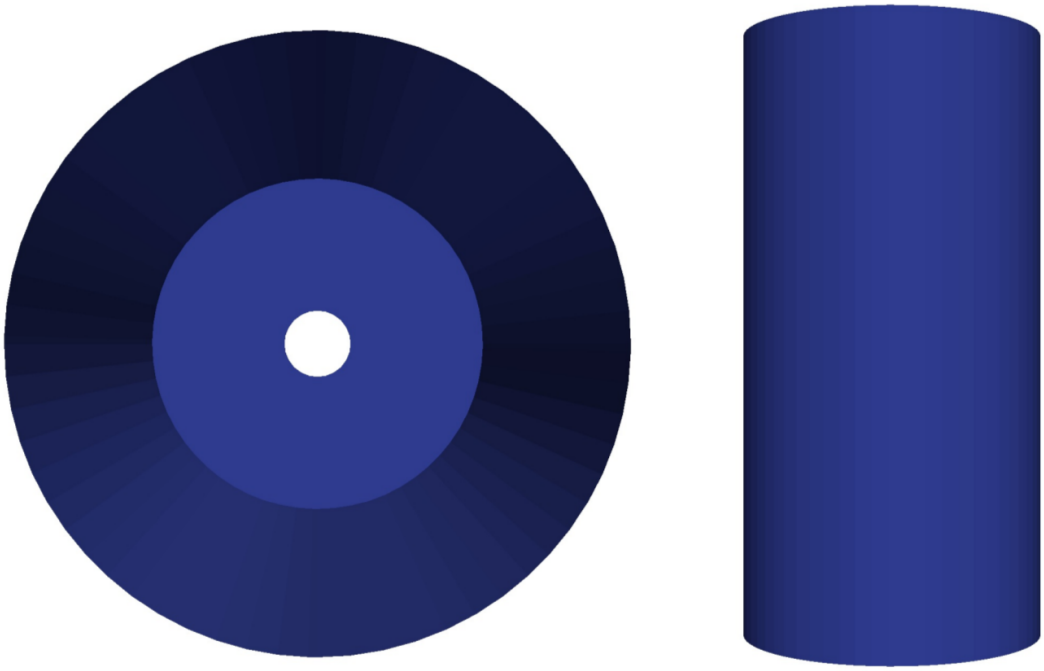

Figure 8: A typical hopper geometry utilized in this thesis. As seen here, the design is essentially an open cylinder with a bottom surface containing the orifice.

3.4 CFD-DEM simulations – the setup and parameters

A hopper flow is realized by first designing a proper hopper geometry using computer-aided design (CAD) tools. The geometry is displayed in Fig. 8. Best described as a hollow cylinder-shaped bucket with an exit hole (orifice) at the bottom, the hopper applied in these simulations has a diameter of $D = 5.0$ cm and an orifice diameter of $D_0 = 1.0$ cm. The bottom of this container (located on the xy-plane) is fixed at $z = 0$ m and the height (measured along z-axis) is set to $h = z = 0.2$ m. This matches the dimensions of a typical hopper used in the experiments. The flow is then initialized by filling the hopper with a closed orifice with granular particles. The location of an individual particle inside the hopper is defined by a pseudorandom number generator and checked for overlaps with other particles. Then, the particles are left to settle onto the hopper by running a DEM-simulation lasting for 0.5 seconds. Finally, either a dry or a submerged simulation is run. The dry granular flow is performed by opening the orifice and running a DEM simulation. The submerged flow is obtained by running the coupled CFD-DEM simulation, where the orifice is opened and the appropriate fluid parameters are set. The computational resources for the simulations were kindly provided by the Aalto Science-IT project.

Modeled as hard-spheres, the granular particles in the simulations are fixed with a Young's modulus of $E = 72$ GPa, a Poisson ratio of $\upsilon = 0.2$, a coefficient of restitution $e = 0.9$ and a (static) friction constant of $\mu_s = 0.1$, which translate to values used in the experiments utilizing silica beads. Furthermore, the particle

density was set to $\rho_{part} = 2500$ kg/m^3 when comparing with the experiments, and $\rho_{part} = 1500$ kg/m^3 otherwise. The latter choice is due to the fact, that the surging effect becomes more apparent in the submerged simulations. The particle diameter is set to $d = 2.0 \pm 0.1$ mm and determined by a Gaussian distribution, so that the error estimate corresponds to a 95 % confidence interval. The particle size distribution is quite monodisperse, which is also reported in the experiments. Smaller particle sizes could also be used, but were neglected in this work due to increased computational costs involved. Additionally, the non-linear Hertz-Mindlin-Dereciewicz contact model is used for a more realistic description of the particle-particle collisions, and the hopper walls share the material properties of the particles as explained above. In the particle-fluid interaction force term (see Sec. 2.5), the most relevant force terms are assumed to be the drag force, the pressure gradient force and the shear stress force.

Furthermore, the fluid is modeled as water, and accordingly, its density is fixed to $\rho_{fluid} = 1000$ kg/m^3 and the kinematic viscosity was varied between $\nu = 10^{-6}$ m^{2}s^{-1} (water at $T = 20°$C), $\nu = 5 \cdot 10^{-6}$ m^{2}s^{-1} and $\nu = 10^{-5}$ m^{2}s^{-1}. No-slip boundary conditions were applied on the surface of the hopper. Both the Di Felice and Koch-Hill drag force models yield almost identical results, which is expected due to the laminar flow conditions (see Appx. B), and therefore, the Di Felice model is used in all simulations.

A typical flow pattern is observed in Fig. 9, in which a series of contour plots drawn at the xz-plane depict the particle volume fraction (red is higher, blue is lower) inside the hopper. At the onset of the flow ($t = 0.5$ s), the hopper is filled with particles. Gradually, the hopper empties as particles exit through the orifice (located at $r = 0.0$ m and $z = 0.0$ m). A typical runtime for such a single simulation consisting approximately $5 \cdot 10^4$ particles is on the order of 8 days while utilizing (the optimal) 24 CPU threads. Therefore, the results displayed in Sec. 4 are obtained from a single run, as obtaining statistics from various initial particle configurations would be a prohibitively time consuming task.

4 Results

Fig. 10 displays the granular discharge rate Q_g as a function of the filling height h in both dry and submerged scenarios as observed in experiments and CFD-DEM simulations. The experiments were kindly planned and conducted by D.Sc. Juha Koivisto of the Department of Physics & Astronomy in the University of Pennsylvania, USA. As seen here, once the flow is initiated, h reduces little by little as particles exit the hopper. Both the experimental and the simulation data seem to be in agreement in the two scenarions both qualitatively and quantitatively. Furthermore, as detailed in the previous section, this agreement is obtained by matching the material properties in the simulation to the literature values of silica beads. This lends credence to the implementation used and suggests that the included terms (drag, pressure gradient and shear stress forces) in the fluid-interaction are sufficient for modeling the scenario. The granular discharge rate also seems to be independent of the filling height in the dry case in the experiments and simulations, thus delightfully

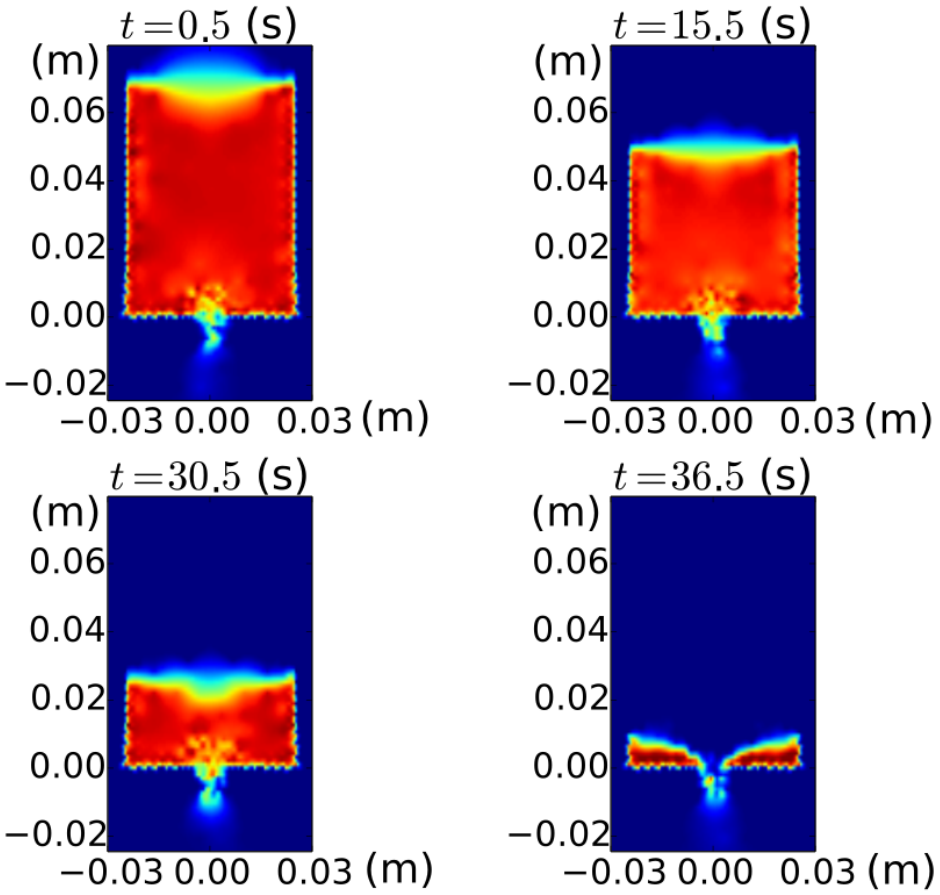

Figure 9: A set of contour plots over the xz-plane ($y = 0.0$ m) taken at various times t, displaying the volume fraction of particles inside a hopper ($D = 5.0$ cm, $D_o = 1.0$ cm). As the hopper flow progresses with increasing time, even more particles have flowed out of the hopper, seen as a decreasing particle volume fraction (red to blue) in the hopper.

agreeing with the prediction set by Eq. 1. Fig. 11 displays additional dry hopper flow simulations, calculated by varying the particle-particle friction coefficient μ, revealing sophisticated behavior of the granular phase. Indeed, in the event of high friction, the Beverloo behavior (Eq. 1) is recovered, but in the case of diminishing friction, the granular discharge rate decreases as h is reduced, thus bearing strong resemblance to a simple (Newtonian) liquid. This indicates that in the low friction scenarios, the free-fall area is not confined to the free-fall arch described above, and is presumably substantially larger. As a result, the discharge rate at the orifice is not only driven by gravity, but also by the pressure imposed by the granular material above the orifice, observed as a strong dependence of Q_g on h.

Additionally, the submerged hopper flow exhibits a more complex character, as Q_g seems to "surge" or increase as the flow progresses in both simulations and experiments, as seen in Fig. 10. To the author's best knowledge, this deviation has been experimentally discovered only recently by Durian *et al.* [13] and the exact

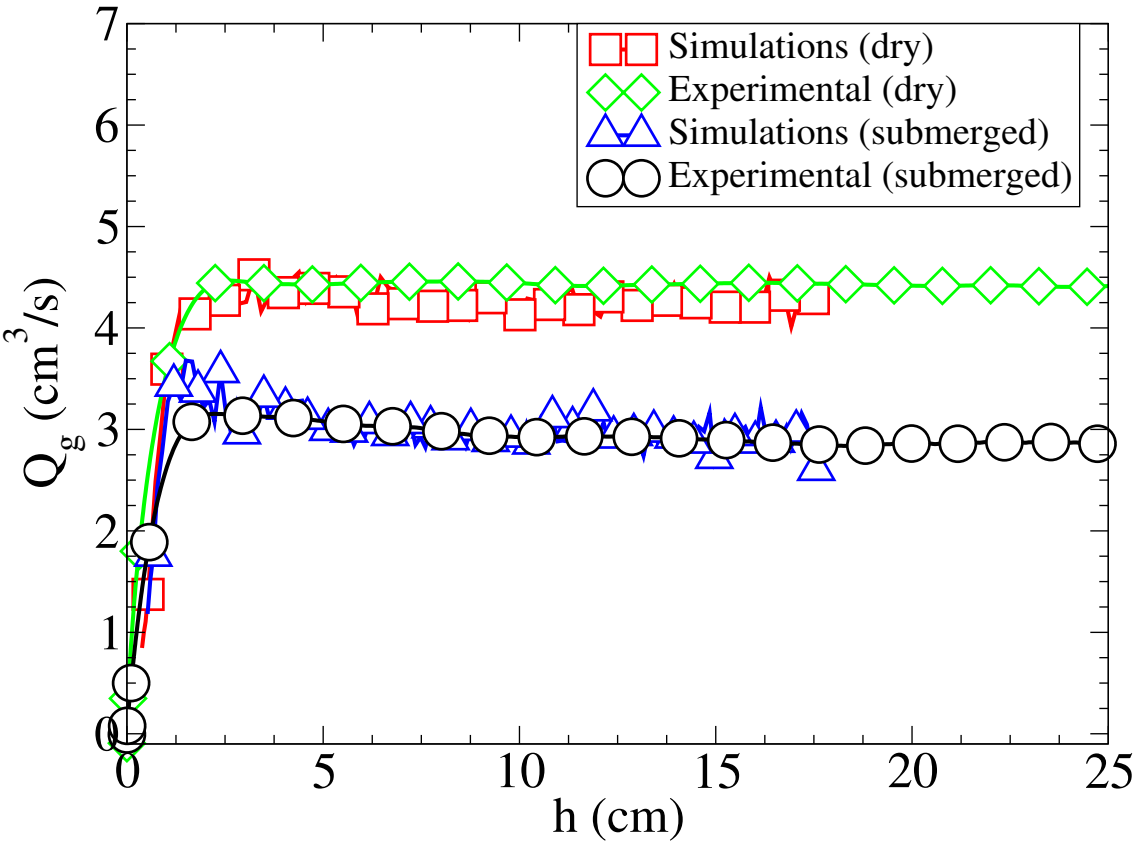

Figure 10: The granular discharge rate Q_g versus the filling height h in a hopper flow (as the hopper empties, the filling height reduces). In both the dry and submerged scenario, both the experiments and the CFD-DEM simulations seem to be in agreement both qualitatively and quantitatively. Furthermore, in the dry hopper discharge, the results agree with Eq. 1 well. However, in both the experiments and simulations, the submerged flow exhibits a granular "surge" as the hopper is emptied, seen as an increased granular discharge rate towards the end.

theoretical explanation is still lacking. This motivates one to study this profound effect in more detail, and is the fundamental focus in the following development.

A reasonable line of inquiry would be to first vary the *fluid* properties independently of the granular particles and observe how the surge is affected. Indeed, Fig. 12 demonstrates the emptying of the hopper as the fluid viscosity is varied while other simulation parameters remain unaltered. As observed here, initially, the granular discharge rate remains lower with increasing fluid viscosity. This seems intuitive, since the fluid now provides increased resistance to the motion of the passing particles, readily seen from the drag force models reviewed in Appx. B. Additionally, it seems that the flux drop is uniform during the flow, *i.e.* the flux decreases the same amount regardless of the filling height. Since varying the viscosity does not appear to effect changes on the surge on a qualitative level, one is inclined to claim that the fluid viscosity is not a fundamental parameter of interest here. This prompts one to explore a different (fluid) property, that is the influx of fluid, in more detail.

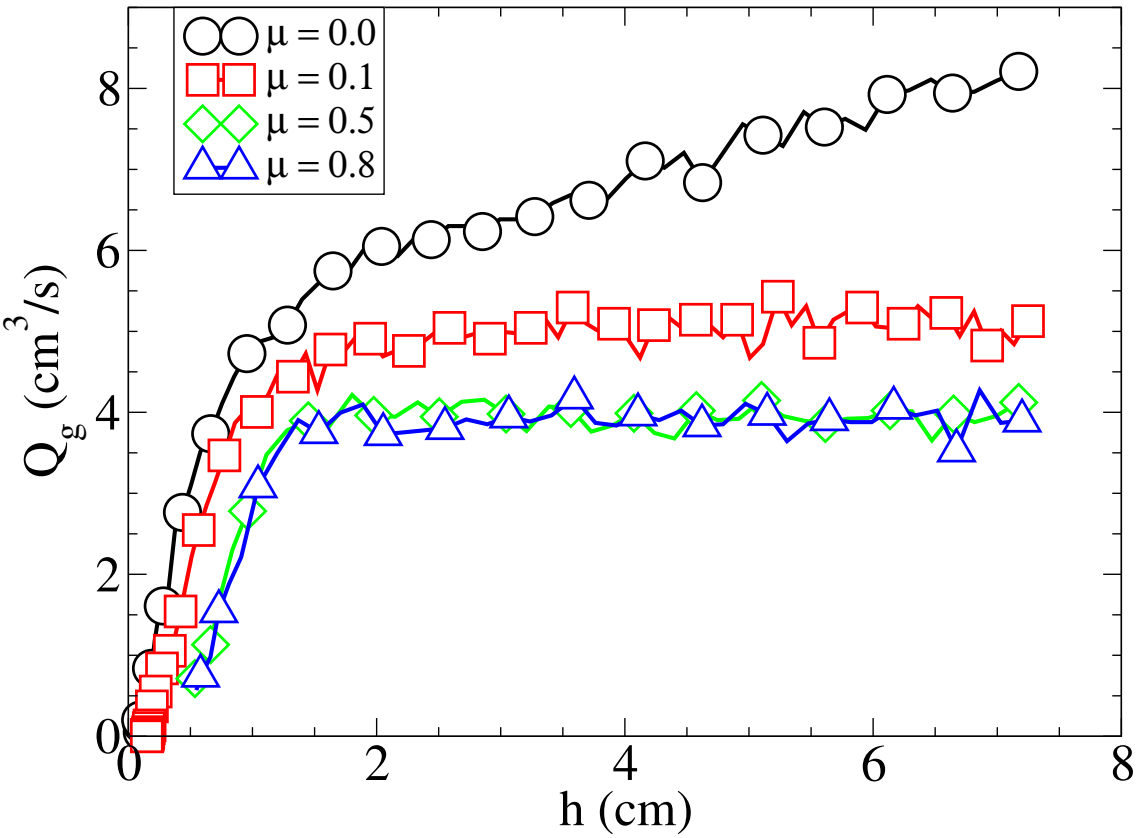

Figure 11: The granular discharge rate Q_g versus the filling height h in a dry hopper flow for various values of the particle-particle static friction coefficient. When the friction is effectively disabled in the system (black curve), the granular phase exits in a similar fashion as a Newtonian liquid. As the static friction coefficient is increased to a minor, but finite value (red curve), Q_g still decreases as h is reduced, albeit less than in the frictionless scenario. As the friction coefficient is increased even more (green and blue curves), the Beverloo behavior is recovered, and Q_g is independent of h.

Accordingly, Fig. 13 depicts the results obtained for an inflow-controlled hopper. As opposed to the reference hopper considered earlier, the top of the hopper is now effectively sealed by a water pump, that imposes a constant influx of water to the hopper, and therefore restricts water from the surroundings from entering the hopper via the hopper top. This scenario is distinctively different from that of the reference (red curve) flow, where the top of the hopper is open. In this free hopper with an open top, the water is freely entering the hopper from the top to counter the water loss at the bottom, that is due to the granular discharge, a direct result of the first Navier-Stokes equation (9) which physically implies the conservation of mass. Depending on the magnitude of the water influx, the hopper may now be "overpumped" or "underpumped" relative to the reference case, meaning the imposed water influx at a given time t may exceed or fall behind of that of the free hopper, where the net water influx is determined by the mass conservation requirement.

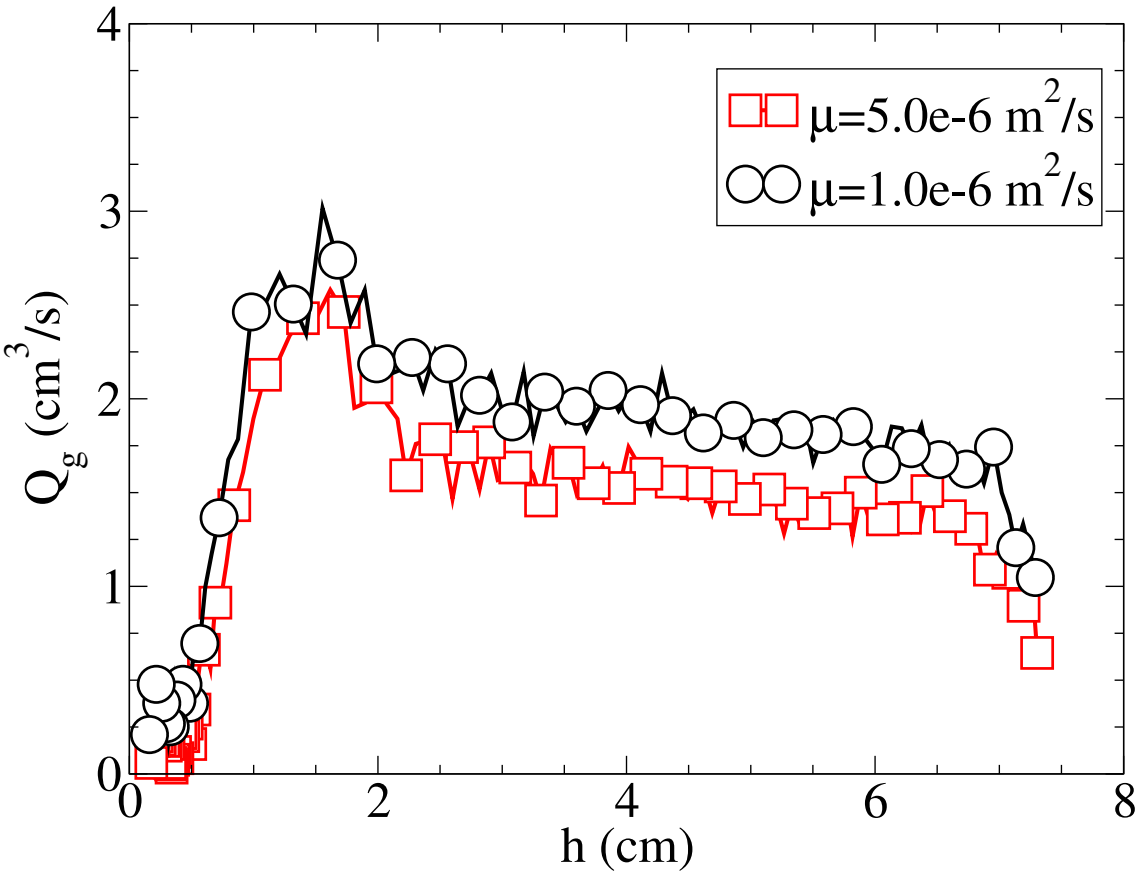

Figure 12: The granular discharge rate Q_g versus the filling height h in a hopper flow (as the hopper empties, the filling height reduces) with varying fluid viscosities. The black line provides the reference (kinematic viscosity of water at room temperature). As the viscosity is increased, the discharge rate drops as the fluid increasingly resists the motion of granular particles, also evident from the drag force models reviewed in Appx. B. However, as the hopper empties, the final surge seems to reach the same peak regardless of the fluid viscosity. This result suggests that the surge is essentially independent of the fluid viscosity.

In Fig. 13, the granular discharge rate is displayed in an overpumped (black curve) and an underpumped case (green curve) while the reference curve (red curve) is also provided for comparison. It is readily observed, that the overpumped hopper provides the highest granular discharge rate Q and the underpumped the lowest throughout the flow, as expected. However, the overpumped flow also exhibits the largest surge, roughly a 100% increase to the initial granular discharge rate, whereas in the reference and underpumped scenarios, this increase is of the order of 40% and 35%, respectively. Accordingly, despite the fact that the influx of water is now strictly controlled, the surge still clearly persists in both overpumped and underpumped cases. Therefore, this would seem to indicate that the possible increase in the water influx of the "free" reference hopper flow, that might occur as the hopper empties, cannot account for the observed surge by itself. Indeed, the surge seems to set in

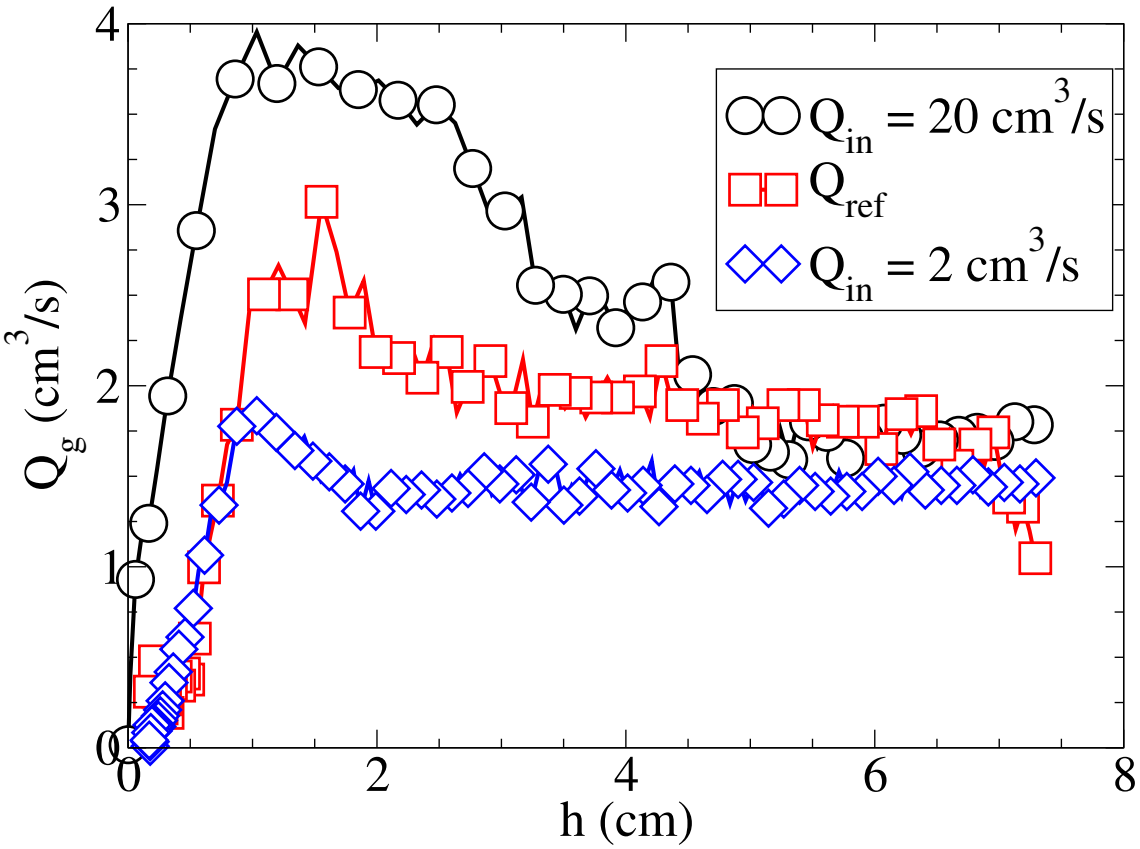

Figure 13: The granular discharge rate Q_g versus the filling height h in a hopper flow (as the hopper empties, the filling height reduces) with controlled fluid inflow. In this scenario, the top of the hopper behaves as a water pump, that restricts the free inflow of water from the surroundings through this top. Instead, it imposes a steady influx of water, that is either "overpumped" or "underpumped" relative to the reference case (red curve), where the top of the hopper remains open, and water is freely entering the hopper to counter the water loss at the bottom of hopper (due to the granular discharge). This is a direct consequence of the first Navier-Stokes equation (9), which physically implies the conservation of mass. The black (green) curve represents an overpumped (underpumped) scenario.

regardless of whether the paramount fluid properties (viscosity, influx) are altered. This prompts one to approach the problem by varying the properties associated with the *granular particles* rather than the fluid.

Indeed, in Fig. 14, the discharge rate is plotted as a function of the filling height for both the linear Hooke contact model (black curve) and the non-linear Hertz-Mindlin-Dereciewicz model (red curve) as detailed in Sec. 2.5. The hopper top is now open ("free" hopper) and the viscosity of water is fixed to that of water. Additionally, the simulation parameters were identical for both models. As seen in the figure, there is a no marked difference in the flux between the two models and once the discharge accelerates, the curves become essentially overlapped. This suggests that the specific contact model has little bearing on the surge qualitatively.

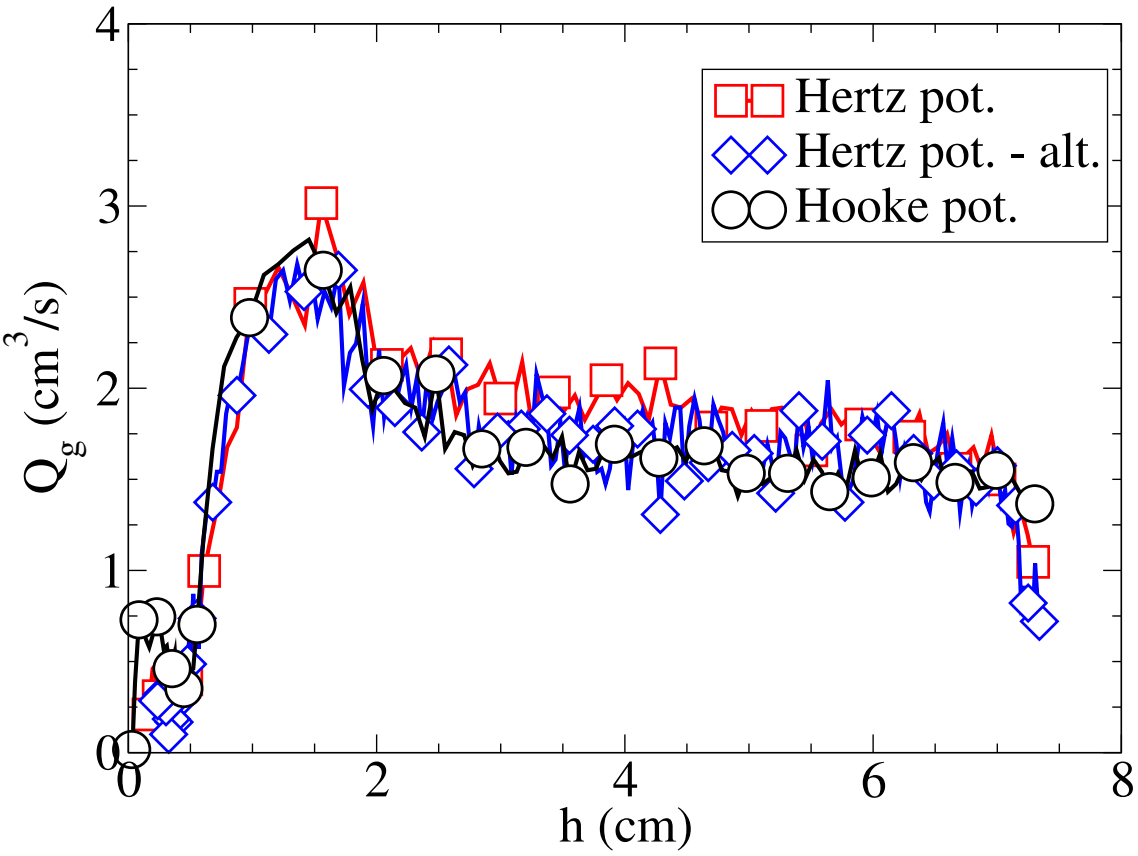

Figure 14: The granular discharge rate Q_g versus the filling height h in a hopper flow (as the hopper empties, the filling height reduces). The black (red) curve represents data obtained with Hookean (Hertz-Mindlin-Dereciewics) contact model, as detailed in Sec. 2.5. For these two datasets, the simulation parameters are fixed to identical values. The green curve depicts data obtained with the HMD-model, but with an altered coefficient of restitution ($e = 0.9$) and Poisson ratio ($\nu = 0.2$). As seen here, both the linear and non-linear contact models yield similar results. There is a slight discrepancy between the flux values in the initial stages of the flow, but once the surge sets in, the data sets become virtually overlapped. Judging by the form of the blue curve, even substantial variations in the values of e and ν effect little change on Q_g.

In addition, the blue curve represents data obtained with the HMD-model as the particle-particle restitution coefficient is increased significantly ($e = 0.9$) and the Poisson ratio decreased ($\nu = 0.2$). Evidently, altering these two material parameters has little impact on the results as no discernible differences are observed. However, manipulating the particle-particle *static friction coefficient* is sufficient to suppress the surge and to an extent, control its magnitude, as seen in the following.

The discharge rate Q_g is plotted as a function of the filling height h for various particle-particle friction coefficients μ in Fig. 15 by applying the full HMD-model. When the friction in the granular bed is effectively disabled (black curve), the flux profile looks flat on average, and the surge is suppressed completely. When μ is

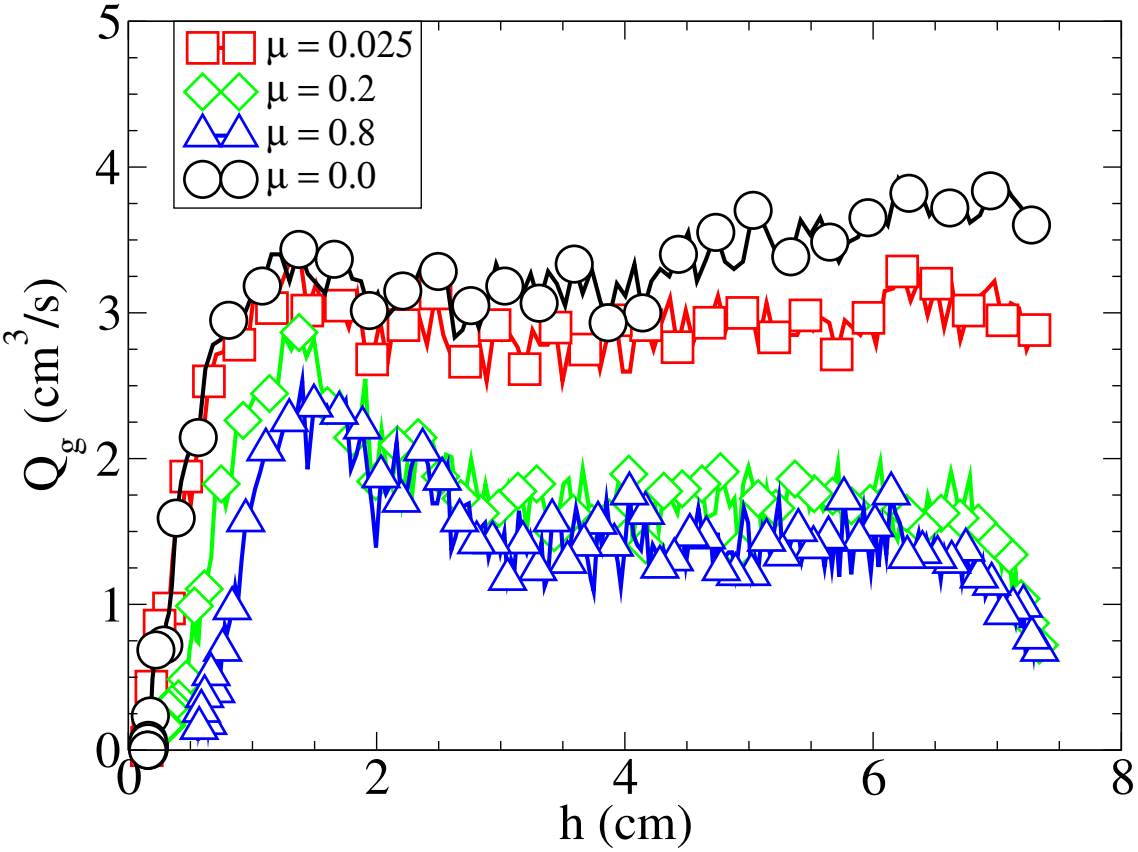

Figure 15: The granular discharge rate Q_g versus the filling height h in a hopper flow for various values of the particle-particle static friction coefficient. When the friction is effectively disabled in the system (black curve), the flux profile seems flat on average and the surge is suppressed throughout the flow, a decidedly different result from the previous ones in this section. As the static friction coefficient is increased to a minor, but finite value (red curve), the surge reappears very subtly. As the friction coefficient is increased even more (green and blue curves), the surge peak becomes more pronounced.

increased to a finite, yet small number (red curve), the surge reappears very subtly. As the friction is increased even further (green and blue curves), the surge peak becomes more pronounced. This would indicate that a finite friction between the particles is a prerequisite for the flux surge and, at least to some extent, its magnitude can be controlled by adjusting the particle-particle friction.

Fig. 16 further explores the results of Fig. 15 for the two cases $\mu = 0$ (no friction) and $\mu = 0.8$ (strong friction) by displaying the mean volume fraction $\langle\phi\rangle$ and the averaged z-component of the velocity $\langle v_z\rangle$ of the particles located at the orifice. The flow progresses from left to right, and the x-axis is scaled to arbitrary time units for better comparison since the flow ceases earlier for the case with negligible friction. Judging by the figure, $\langle\phi\rangle$ is clearly higher for the frictionless system during the flow and the quantity also shows a steady decrease over time, suggesting that the flow pattern inside the hopper lacks the free-fall arch introduced earlier and the actual

free-fall zone of these frictionless particles is considerably larger, as in the case of dry hopper flows presented earlier. This interpretation is also supported by the fact that the magnitude of $\langle v_z \rangle$ for the particles in the frictionless case are consistently higher than for those in the system with strong frictional interactions. In addition, the particle ensemble with strong friction displays a transient, as $\langle \phi \rangle$ grows steadily in the initial stages of the flow, and finally attains a constant value that is sustained throughout the flow. This suggests that the free-fall arch is formed gradually inside the hopper and sustained in this high friction scenario.

Finally, Fig. 17 displays the mean fluid velocity $\langle U_z \rangle$ in the z-direction for the friction coefficients $\mu = 0$, $\mu = 0.2$ and $\mu = 0.8$ during the flow in arbitrary time units. As seen here, the averaged fluid velocity in the z-direction also surges as the flow evolves in time. This figure also reveals a remarkable result, as the fluid velocities seem to reach the exact same maximum peak (surge) regardless of μ, suggesting that the surge in the fluid phase is a robust feature, influenced only by the necessary condition of the fluid having to replace lost volume at the bottom of the hopper as the granular particles exit via the orifice, a direct consequence of the first Navier-Stokes equation reviewed in Sec. 2.2. This condition also offers a plausible explanation for the surge phenomenon of both the fluid and the granular phase. As such, the exiting granular phase "pumps" the liquid via the top of the hopper. However, in the initial and intermittent stages of the flow, the granular bed remains rather thick and the ability of the liquid to penetrate this porous layer is limited, as described by Darcy's law [61]. As a result, a pressure difference develops between the top and the orifice of the hopper. However, once the hopper empties sufficiently and the granular bed reaches a characteristic length scale, this pressure difference suddenly relaxes and as a result, the fluid velocity surges. Whether the granular phase also surges or not, is entirely dependent on the relative velocities of these two phases. Judging by Figs. 16 and 17, the free-fall area of the frictionless particle system is considerably larger than that confined by a free-fall arch, and the particles have a fairly consistent and large mean velocity in the z-direction, $\langle v_z \rangle \approx 8.5$–$10$ cm/s. Subsequently during surging, the fluid phase never quite reaches this threshold, and as a result no surge in the granular phase is observed. In the case of a strong friction, however, the presence of the free-fall arch decreases the free-fall zone of the granular particles substantially, and $\langle v_z \rangle$ is appreciably lower, around 5-6 cm/s. However, once the fluid phase surges, it reaches the peak magnitude of 8 cm/s and is actually proceeding faster than the granular phase, and the drag imposed by the liquid does no longer hinder the movement of the granular phase, but *enhances* it. As a result, the granular phase also exhibits a strong surge and a subsequent increase in the granular discharge rate is observed as well.

5 Discussion

Granular systems are ubiquitous in the world, spanning a wide range of materials from natural sands and slurries to powders in the food industry. Especially in this setting, the granular media are regularly stored in containers (*e.g.* grain silos, dosing

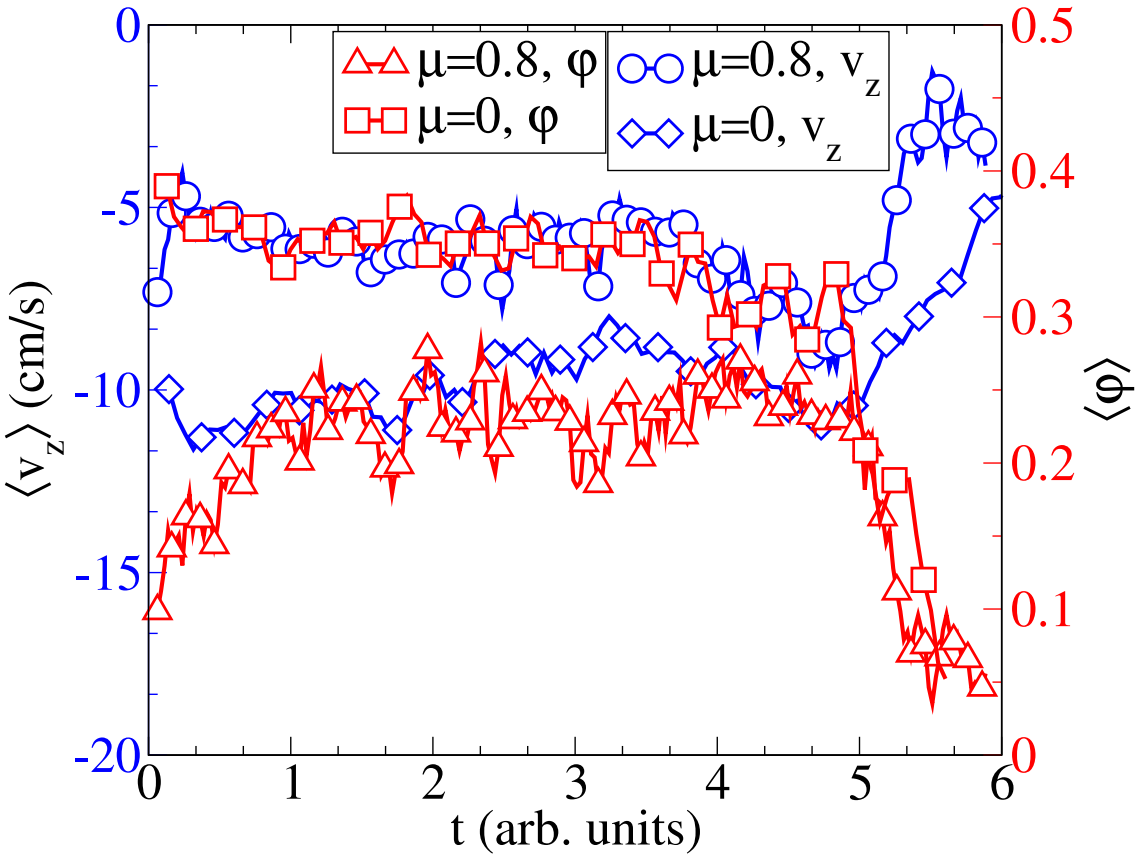

Figure 16: The mean volume fraction $\langle\phi\rangle$ and the averaged z-component of the velocity $\langle v_z\rangle$ of the particles located at the orifice during the submerged hopper flow for $\mu = 0$ and $\mu = 0.8$. The flow progresses from left to right in time. Additionally, since it persists longer for $\mu = 0.8$, the x-axis has been scaled for better comparison. As seen here, $\langle\phi\rangle$ is larger for $\mu = 0$ (red curve with squares) during the flow and it decreases monotonically as the flow progresses, suggesting that the frictionless case lacks the free-fall arch structure introduced earlier, and the free-fall zone is actually considerably larger in the frictionless scenario. This conclusion is also supported by the fact that the average velocity in the z-direction for $\mu = 0$ (blue curve with diamonds) is evidently larger as well. Meanwhile, strong friction ($\mu = 0.8$) introduces a transient to $\langle\phi\rangle$ in the initial stages of the flow, during which the orifice becomes saturated with particles and the free-fall arch is slowly formed (red curve with triangles). Then, unlike for $\mu = 0$, $\langle\phi\rangle$ stays nearly constant up until the flow ceases, which is yet another signature of the presence of a well-defined free-fall arch.

containers) that resemble the hopper geometry, (here) a hollow cylinder with an open top and an orifice at the bottom. If the axis of the cylindrical hopper is aligned with the gravitational force and the orifice is opened, a granular hopper flow ensues and is maintained by the gravitational force that imposes stress on the media. In the event of negligible interactions with the surrounding interstitial fluid, such as air, the granular discharge rate of such flow is given by the Beverloo equation. This equation implies that the rate is independent of the filling height, *i.e.* the height of

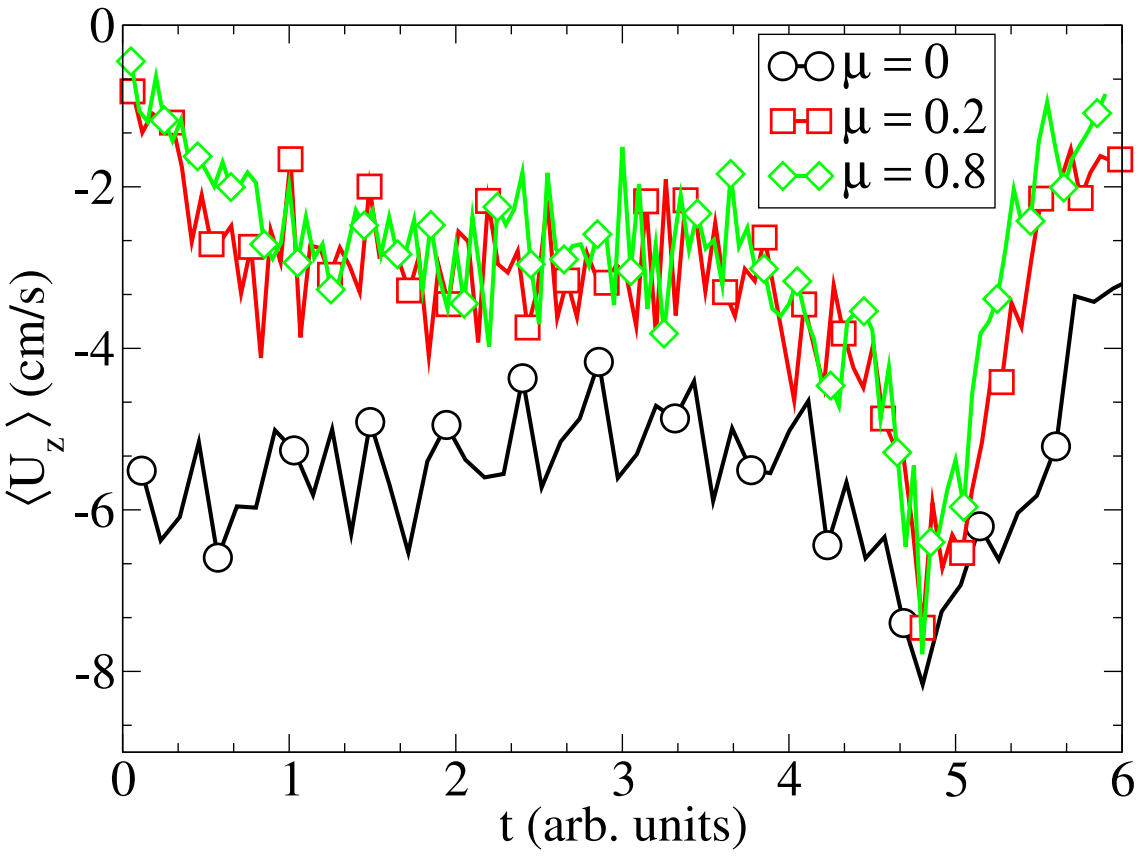

Figure 17: The mean fluid velocity in the z-direction $\langle U_z \rangle$ for various μ as the flow evoles in time (in arbitrary units). As seen here, the fluid phase also exhibits a surge towards the end of the flow. Remarkably, the surge peaks are independent of μ, a clearly distinct feature from the surging of the granular phase seen in Fig. 15. This suggests that the surge in the fluid phase is a robust feature, that is only determined by the necessary condition of the fluid phase having to replace lost volume at the bottom of the hopper as granular particles exit via the orifice.

the granular bed in the hopper.

However, in recent experimental studies conducted by Durian *et al.*, a hopper was submerged in a liquid and consequently, both the hopper and the granular media inside it were embedded in a liquid. Subsequently, the hopper flow in such a setup displayed a surprising dependence between the granular discharge rate Q_g and the filling height h. As the flow progressed and the hopper emptied, this rate surged (accelerated) towards the end. Up until recently, there had been no theoretical treatment of the subject and it was the aim of this thesis to model this submerged hopper flow. Specifically, the objective was to reproduce the experimental results by computational methods and offer a valid explanation for the surge observed in the granular discharge rate.

The approach adopted in this thesis relied on modeling the submerged hopper flow as a two-phase system, where the fluid phase is described on a continuum level and the granular phase on a discrete level. Thus, the fluid phase was modeled

by solving the Navier-Stokes (NS) equations in a Computational Fluid Dynamics (CFD) framework, that was coupled the granular phase, which was represented by the Discrete Element Method (DEM), where each granular particle is tracked individually by solving Newton's 2nd law. This coupling was realized by modifying the original NS equations, and introducing a fluid-particle interaction term to both the 2nd NS equation and the Newton's 2nd law for each particle. This interaction term may include drag forces, buoyancy and pressure gradient forces, for instance. By choosing suitable simulation parameters, reasonable agreement between the experimental data and the simulations was obtained. Additionally, a finite particle-particle static friction coefficient μ was a prerequisite for the surge to occur, and to some extent, the magnitude of the surge could be directly controlled by altering this parameter.

A further examination of the results revealed that the exiting granular phase "pumps" the liquid into the hopper via the open hopper top, since the first Navier-Stokes equation necessitates that the fluid phase replace the volume lost at the bottom of the hopper due to granular particles exiting through the orifice. However, since the ability of the fluid phase to penetrate the porous medium is limited (as inferred from Darcy's law), a pressure difference developed between the top and the orifice region of the hopper. This pressure difference suddenly relaxed as the granular bed grew sufficiently thin during the flow, and as a result, the fluid phase surged, observed as a sizable increase in the average fluid velocity $\langle U_z \rangle$ at the orifice. Then, this surge might or might not induce a surge onto the granular phase as well, depending on the relative velocities. In the case of a non-existent friction, the effective free-fall area of the granular particles was large, and their mean velocity in the z-direction $\langle v_z \rangle$ at the orifice was substantially larger compared to the system with strong frictional interactions. As a result, regardless of the surge, the fluid phase never reached these values and continued to hinder the movement of the granular particles (drag force). In the case of strong friction, on the other hand, the free-fall area of the particles was contained to a small volume defined by the free-fall arch, and consequently, $\langle v_z \rangle$ remained relatively small at the orifice, though larger than the respective mean fluid velocity $\langle U_z \rangle$ in the initial and intermittent stages of the flow. However, once the fluid phase surged, $\langle U_z \rangle$ actually surpassed the value of $\langle v_z \rangle$, and therefore the drag imposed by the liquid enhanced the movement of the granular particles through the orifice, seen as a surging of the granular phase as well.

References

[1] P.-G. de Gennes. Granular matter: a tentative view. *Reviews of Modern Physics*, 71(2):S374, 1999.

[2] P. Jop, Y. Forterre, and O. Pouliquen. A constitutive law for dense granular flows. *Nature*, 441(7094):727–730, 2006.

[3] H.M. Jaeger, S.R. Nagel, and R.P. Behringer. Granular solids, liquids, and gases. *Reviews of Modern Physics*, 68(4):1259, 1996.

[4] I.S. Aranson and L.S. Tsimring. Patterns and collective behavior in granular media: Theoretical concepts. *Reviews of Modern Physics*, 78(2):641, 2006.

[5] Y. Forterre and O. Pouliquen. Flows of dense granular media. *Annual Review of Fluid Mechanics*, 40:1–24, 2008.

[6] C.S. Campbell. Granular material flows–an overview. *Powder Technology*, 162(3):208–229, 2006.

[7] L.P. Kadanoff. Built upon sand: Theoretical ideas inspired by granular flows. *Reviews of Modern Physics*, 71(1):435, 1999.

[8] I. Goldhirsch. Rapid granular flows. *Annual review of fluid mechanics*, 35(1):267–293, 2003.

[9] P.W. Cleary and M.L. Sawley. DEM modelling of industrial granular flows: 3D case studies and the effect of particle shape on hopper discharge. *Applied Mathematical Modelling*, 26(2):89–111, 2002.

[10] A. Janda, D. Maza, A. Garcimartín, E. Kolb, J. Lanuza, and E. Clément. Unjamming a granular hopper by vibration. *Europhysics Letters*, 87(2):24002, 2009.

[11] T. Iqbal and J.J. Fitzpatrick. Effect of storage conditions on the wall friction characteristics of three food powders. *Journal of Food Engineering*, 72(3):273–280, 2006.

[12] J.J. Fitzpatrick, T. Iqbal, C. Delaney, T. Twomey, and M.K. Keogh. Effect of powder properties and storage conditions on the flowability of milk powders with different fat contents. *Journal of Food Engineering*, 64(4):435–444, 2004.

[13] T.J. Wilson, C.R. Pfeifer, N. Meysingier, and D.J. Durian. Granular discharge rate for submerged hoppers. *Papers in Physics*, 6(2):0–0, 2014.

[14] C. Mankoc, A. Janda, R. Arevalo, J.M. Pastor, I. Zuriguel, A. Garcimartín, and D. Maza. The flow rate of granular materials through an orifice. *Granular Matter*, 9(6):407–414, 2007.

[15] L. Staron, P.Y. Lagrée, and S. Popinet. The granular silo as a continuum plastic flow: The hour-glass vs the clepsydra. *Physics of Fluids (1994-present)*, 24(10):103301, 2012.

[16] J.E. Hilton and P.W. Cleary. Granular flow during hopper discharge. *Physical Review E*, 84(1):011307, 2011.

[17] P. Lin, S. Zhang, J. Qi, Y.M. Xing, and L. Yang. Numerical study of free-fall arches in hopper flows. *Physica A: Statistical Mechanics and its Applications*, 417:29–40, 2015.

[18] A. Janda, I. Zuriguel, and D. Maza. Flow rate of particles through apertures obtained from self-similar density and velocity profiles. *Physical Review Letters*, 108(24):248001, 2012.

[19] S.M. Rubio-Largo, A. Janda, D. Maza, I. Zuriguel, and R.C. Hidalgo. Disentangling the free-fall arch paradox in silo discharge. *Physical Review Letters*, 114(23):238002, 2015.

[20] J.E. Hilton, L.R. Mason, and P.W. Cleary. The effect of gas dynamics on hopper discharge rates. In *Proceedings of the 7th International Conference on CFD in the Minerals and Process Industries*, 2009.

[21] H.P. Zhu, Z.Y. Zhou, R.Y. Yang, and A.B. Yu. Discrete particle simulation of particulate systems: theoretical developments. *Chemical Engineering Science*, 62(13):3378–3396, 2007.

[22] P.A. Cundall and O.D.L. Strack. A discrete numerical model for granular assemblies. *Geotechnique*, 29(1):47–65, 1979.

[23] Z.Y. Zhou, S.B. Kuang, K.W. Chu, and A.B. Yu. Discrete particle simulation of particle–fluid flow: model formulations and their applicability. *Journal of Fluid Mechanics*, 661:482–510, 2010.

[24] T.B. Anderson and R. Jackson. Fluid mechanical description of fluidized beds. Equations of motion. *Industrial & Engineering Chemistry Fundamentals*, 6(4):527–539, 1967.

[25] M. Ishii and T. Hibiki. *Thermo-fluid dynamics of two-phase flow*. Springer Science & Business Media, 2010.

[26] F.A. Morrison. *Understanding rheology*. Oxford University Press, USA, 2001.

[27] H. Jasak. *Error analysis and estimation for the finite volume method with applications to fluid flows*. PhD thesis, Imperial College, University of London, June 1996.

[28] G.J. Pert. *Introductory fluid mechanics for physicists and mathematicians*. John Wiley & Sons, 2013.

[29] C.L. Fefferman. Existence and smoothness of the Navier-Stokes equation. *The millennium prize problems*, pages 57–67, 2000.

[30] J. Tu, G. H. Yeoh, and C. Liu. *Computational fluid dynamics: a practical approach*. Butterworth-Heinemann, 2012.

[31] J.H. Ferziger and M. Peric. *Computational methods for fluid dynamics*. Springer Science & Business Media, 2012.

[32] H. Hirsch. Numerical computation of internal and external flows. *Computational Methods for Inviscid and Viscous Flows*, 2:536–556, 1990.

[33] R.I. Issa. Solution of the implicitly discretised fluid flow equations by operator-splitting. *Journal of Computational Physics*, 62(1):40–65, 1986.

[34] L. Vu-Quoc and X. Zhang. An accurate and efficient tangential force–displacement model for elastic frictional contact in particle-flow simulations. *Mechanics of Materials*, 31(4):235–269, 1999.

[35] N.G. Deen, M.V.S. Annaland, M.A. Van der Hoef, and J.A.M. Kuipers. Review of discrete particle modeling of fluidized beds. *Chemical Engineering Science*, 62(1):28–44, 2007.

[36] B.P.B. Hoomans, J.A.M. Kuipers, W.J. Briels, and W.P.M. Van Swaaij. Discrete particle simulation of bubble and slug formation in a two-dimensional gas-fluidised bed: a hard-sphere approach. *Chemical Engineering Science*, 51(1):99–118, 1996.

[37] W.C. Swope, H.C. Andersen, P.H. Berens, and K.R. Wilson. A computer simulation method for the calculation of equilibrium constants for the formation of physical clusters of molecules: Application to small water clusters. *The Journal of Chemical Physics*, 76(1):637–649, 1982.

[38] C. Goniva, C. Kloss, N.G. Deen, J.A.M. Kuipers, and S. Pirker. Influence of rolling friction on single spout fluidized bed simulation. *Particuology*, 10(5):582–591, 2012.

[39] K.D. Kafui, C. Thornton, and M.J. Adams. Discrete particle-continuum fluid modelling of gas–solid fluidised beds. *Chemical Engineering Science*, 57(13):2395–2410, 2002.

[40] I.E. Barton. Computation of particle tracks over a backward-facing step. *Journal of Aerosol Science*, 26(6):887–901, 1995.

[41] J. Tu, K. Inthavong, and G. Ahmadi. *Computational fluid and particle dynamics in the human respiratory system*. Springer Science & Business Media, 2012.

[42] H. Pérez-de Tejada. Magnus force in the Venus ionosphere. *Journal of Geophysical Research: Space Physics (1978–2012)*, 111(A11), 2006.

[43] S. Ergun. Fluid flow through packed columns. *Chemical Engineering Progress*, 48, 1952.

[44] C. Wen and Y.H. Yu. Mechanics of fluidization. In *The Chemical Engineering Progress Symposium Series*, volume 62, page 100, 1966.

[45] R. Di Felice. The voidage function for fluid-particle interaction systems. *International Journal of Multiphase Flow*, 20(1):153–159, 1994.

[46] D.L. Koch and R.J. Hill. Inertial effects in suspension and porous-media flows. *Annual Review of Fluid Mechanics*, 33(1):619–647, 2001.

[47] H. Hertz. Ueber die Berührung fester elastischer Körper. *Journal für die reine und angewandte Mathematik*, 92:156–171, 1882.

[48] R.D. Mindlin and H. Deresiewicz. Elastic spheres in contact under varying oblique forces. *Transactions of ASME, Series E*, 20:327–344, 1953.

[49] A. Di Renzo and F.P. Di Maio. Comparison of contact-force models for the simulation of collisions in DEM-based granular flow codes. *Chemical Engineering Science*, 59(3):525–541, 2004.

[50] P.A. Langston, U. Tüzün, and D.M. Heyes. Discrete element simulation of granular flow in 2D and 3D hoppers: dependence of discharge rate and wall stress on particle interactions. *Chemical Engineering Science*, 50(6):967–987, 1995.

[51] Y.C. Zhou, B.D. Wright, R.Y. Yang, B.H. Xu, and A.B. Yu. Rolling friction in the dynamic simulation of sandpile formation. *Physica A: Statistical Mechanics and its Applications*, 269(2):536–553, 1999.

[52] N.V. Brilliantov and T. Pöschel. Rolling friction of a viscous sphere on a hard plane. *Europhysics Letters*, 42(5):511, 1998.

[53] *OpenFoam: The OpenSource CFD Toolbox, User Guide*. OpenFoam Foundation, 2014.

[54] F. Inok, A. Lavrov, and C.G. Soares. Analysis of complex fluid flow test cases with OpenFOAM. *Developments in Maritime Transportation and Exploitation of Sea Resources: IMAM 2013*, page 183, 2013.

[55] C. Peralta, H. Nugusse, S.P. Kokilavani, J. Schmidt, and B. Stoevesandt. Validation of the simpleFoam (RANS) solver for the atmospheric boundary layer in complex terrain. In *ITM Web of Conferences*, volume 2, page 01002. EDP Sciences, 2014.

[56] H. Nilsson. Some experiences on the accuracy and parallel performance of OpenFOAM for CFD in water turbines. In *Applied Parallel Computing. State of the Art in Scientific Computing*, pages 168–176. Springer, 2007.

[57] D.A. Lysenko, I.S. Ertesvåg, and K.E. Rian. Modeling of turbulent separated flows using OpenFOAM. *Computers & Fluids*, 80:408–422, 2013.

[58] C. Kloss, C. Goniva, A. Hager, S. Amberger, and S. Pirker. Models, algorithms and validation for opensource DEM and CFD–DEM. *Progress in Computational Fluid Dynamics, an International Journal*, 12(2-3):140–152, 2012.

[59] S. Plimpton. Fast parallel algorithms for short-range molecular dynamics. *Journal of Computational Physics*, 117(1):1–19, 1995.

[60] R. Berger, C. Kloss, A. Kohlmeyer, and S. Pirker. Hybrid parallelization of the LIGGGHTS open-source DEM code. *Powder Technology*, 278:234–247, 2015.

[61] M. Firdaouss, J.-L. Guermond, and P. Le Quéré. Nonlinear corrections to Darcy's law at low Reynolds numbers. *Journal of Fluid Mechanics*, 343:331–350, 1997.

[62] H. Enwald, E. Peirano, and A.E. Almstedt. Eulerian two-phase flow theory applied to fluidization. *International Journal of Multiphase Flow*, 22:21–66, 1996.

[63] T. Kambe. *Elementary fluid mechanics*, volume 258. World Scientific, 2007.

[64] R. Beetstra, M.A. Van der Hoef, and J.A.M. Kuipers. Drag force of intermediate Reynolds number flow past mono-and bidisperse arrays of spheres. *AIChE Journal*, 53(2):489–501, 2007.

[65] W. Du, X. Bao, J. Xu, and W. Wei. Computational fluid dynamics (CFD) modeling of spouted bed: Assessment of drag coefficient correlations. *Chemical Engineering Science*, 61(5):1401–1420, 2006.

[66] J. Happel and H. Brenner. *Low Reynolds number hydrodynamics: with special applications to particulate media*, volume 1. Springer Science & Business Media, 2012.

A Deriving the two-phase Navier-Stokes mass and momentum equations

Reframing the original Navier-Stoke equations (Eqs. 9 and 10) to accomodate a solid phase requires extensive utilization of the weighing function g introduced in Sec. 2.4. In the following, the individual terms in these equations are weighed by g and spatially integrated over the fluid volume term by term to yield the modified NSEs. These then describe the fluid properties in terms of spatially averaged quantities, rather than the point quantities observed in Eqs. 9 and 10. Essentially, this description models the fluid phase in a system consisting of two interpenetrating media (fluid and solid).

To begin with, the integral, defining the fluid (subscript fl) volume fraction ϵ at point $\mathbf{x}$ and time t is defined as [24]

$$\epsilon(\mathbf{x},t) = \int_{V_{fl\infty}(t)} g(\mathbf{x}-\mathbf{y})dV_y. \tag{A1}$$

$V_{fl\infty}$ indicates that this integral is taken over all points $\mathbf{y}$ occupied by the fluid at time t and dV_y denotes the fluid volume near $\mathbf{y}$. Additionally, if a' denotes any fluid point property, such as p or $\mathbb{T}$ in Eq. 10, its local mean value a at $(\mathbf{x},t)$ is defined by [24]

$$\epsilon(\mathbf{x},t)a(\mathbf{x},t) = \int_{V_{fl\infty}(t)} a'(\mathbf{y},t)g(\mathbf{x}-\mathbf{y})dV_y. \tag{A2}$$

By examining Eq. A2, one might conclude that the local mean values are not unique, since g can possess an arbitrary form and, more importantly, an arbitrary radius (as defined earlier), which defines the region of integration. However, the situation simplifies reasonably once an important assumption is made: any spatial variations in a local point property are significantly affected by only two length scales, a scale comparable to particle spacing and a much larger scale proportionate to the system dimensions. If the radius of g is chosen so that it is considerably larger than the former scale yet small compared to the latter, the local averages have an unambigous physical meaning [24]. An important consequence of this is the following result [24]

$$\int_{V_{fl\infty}(t)} a(\mathbf{y},t)g(\mathbf{x}-\mathbf{y})dV_y \approx a(\mathbf{x},t)\int_{V_{fl\infty}(t)} g(\mathbf{x}-\mathbf{y})dV_y = \epsilon(\mathbf{x},t)a(\mathbf{x},t). \tag{A3}$$

Note that due to the length scales introduced above, the following development specifically excludes scenarios, in which strong, discontinuos fluctuations in the flow quantities exist within the characteristic length scale of the averaging volume, *i.e.* smooth behavior of these quantities in the volume is expected.

Next, still pursuing Eq. 10 formulated in local mean quantities, the local mean values have to be established for quantities undergoing partial differentiation. Examining Eq. 10 reveals that partial derivatives with respect to both time t and place x_k have to be addressed. Starting with the latter, the Gauss's theorem, first introduced in Sec. 2.3, is rewritten in a componentwise manner [62]

$$\int_V \frac{\partial}{\partial x_k} f dV = \int_A f n_k dA, \tag{A4}$$

where n_k denotes the boundary normal to the surface. Note that here, the summation over k (the full divergence operation) has been suppressed in the notation, a convention used throughout this appendix. Now, differentiating Eq. A2 with respect to position and applying Eq. A4 yields

$$\frac{\partial}{\partial x_k}\int_{V_{fl\infty}(t)} a'(\mathbf{y},t)g(\mathbf{x}-\mathbf{y})dV_y = \int_{V_{fl\infty}(t)} g(\mathbf{x}-\mathbf{y})\frac{\partial a'(\mathbf{y},t)}{\partial y_k}dV_y - \int_{S_{fl}(t)} n_k a'(\mathbf{y},t)g(\mathbf{x}-\mathbf{y})dS_y, \tag{A5}$$

where n_k now denotes the boundary (outward) normal to the fluid and the relation [24]

$$\frac{\partial}{\partial x_k}g(\mathbf{x}-\mathbf{y}) = -\frac{\partial}{\partial y_k}g(\mathbf{x}-\mathbf{y}) \tag{A6}$$

has been used in the second term of the right-hand side. Note that $S_{fl}(t)$ refers to the (disjoint) fluid surfaces over the $S_{fl\infty}$ bounding the whole system. If we designate $s_p(t)$ as the surface of a separate solid particle at time t, the second term in Eq. A5 can be intuitively expressed as [24]

$$\int_{S_{fl}(t)} n_k a'(\mathbf{y},t)g(\mathbf{x}-\mathbf{y})dS_y = \int_{S_{fl\infty}} n_k a'(\mathbf{y},t)g(\mathbf{x}-\mathbf{y}) - \sum_{p\infty}\int_{s_p(t)} n_k a'(\mathbf{y},t)g(\mathbf{x}-\mathbf{y})dS_y. \tag{A7}$$

In Eq. A7, provided that r_0 is negligibly small compared to the shortest distance from the point $\mathbf{x}$ to the surface $S_{fl\infty}$, the first right-hand side term can be ignored as it contributes very little. Plugging this result to Eq. A5 yields the final result [24]

$$\int_{V_{fl\infty}(t)} g(\mathbf{x}-\mathbf{y})\frac{\partial a'(\mathbf{y},t)}{\partial y_k}dV_y = \frac{\partial}{\partial x_k}[\epsilon(\mathbf{x},t)a(\mathbf{x},t)] - \sum_{p\infty}\int_{s_p(t)} a'(\mathbf{y},t)n_k g(\mathbf{x}-\mathbf{y})dS_y, \tag{A8}$$

which is the local average expression for a spatially differentiated quantity $\partial a'/\partial y_k$. For the differentiation with respect to time, Eq. A2 is first differentiated with respect to time and then, Leibnitz's theorem [62] is used to yield

$$\frac{\partial}{\partial t}[\epsilon(\mathbf{x},t)a(\mathbf{x},t)] = \int_{V_{fl\infty}(t)} g(\mathbf{x}-\mathbf{y})\frac{\partial a'(\mathbf{y},t)}{\partial t}dV_y - \int_{S_{fl}(t)} n_k u'_k a'(\mathbf{y},t)g(\mathbf{x}-\mathbf{y})dS_y, \tag{A9}$$

where u'_k is the local fluid velocity. Following the exact reasoning as demonstrated above for $\partial/\partial x_k$, the final result reads [24]

$$\int_{V_{fl\infty}(t)} g(\mathbf{x}-\mathbf{y})\frac{\partial a'(\mathbf{y},t)}{\partial t}dV_y = \frac{\partial}{\partial t}[\epsilon(\mathbf{x},t)a(\mathbf{x},t)] + \sum_{p\infty}\int_{s_p(t)} a'(\mathbf{y},t)n_k u'_k(\mathbf{y},t)g(\mathbf{x}-\mathbf{y})dS_y. \tag{A10}$$

With the above development, Eq. 9 can now be reframed in a two-phase system. Multiplying the original equation by the weighing function g and integrating clearly yields [24]

$$\int_{V_{fl\infty}} g(\mathbf{x}-\mathbf{y})\frac{\partial u'(\mathbf{y},t)}{\partial y_k}dV_y = 0. \tag{A11}$$

Note that here, the formula has been converted to component-wise presentation, again suppressing summations for convenience. This expression can be manipulated with the aid of Eq. A8 to state

$$\frac{\partial}{\partial x_k}\left[\epsilon(\mathbf{x},t)u(\mathbf{x},t)\right] = \sum_{p\infty}\int_{s_p(t)} u'(\mathbf{y},t)n_k g(\mathbf{x}-\mathbf{y})dS_y. \tag{A12}$$

On the other hand, setting $a' = 1$ (and $a = 1$ as observed in Eq. A2) in Eq. A10 amounts to

$$\frac{\partial}{\partial t}\epsilon(\mathbf{x}) = -\sum_{p\infty}\int_{s_p(t)} u'(\mathbf{y},t)n_k g(\mathbf{x}-\mathbf{y})dS_y. \tag{A13}$$

By adding Eqs. A12 and A13 together, the first NS equation for the fluid phase in a two-phase system is conveniently obtained [24]

$$\frac{\partial \epsilon}{\partial t} + \frac{\partial}{\partial x_k}(\epsilon u_k) = 0. \tag{A14}$$

Concurrently, Eq. 10 can also be expressed in terms of local averages. Multiplying by $g(\mathbf{x}-\mathbf{y})$ and integrating results in

$$\begin{aligned}\rho_{fl}\int_{V_{fl\infty}} g(\mathbf{x}-\mathbf{y})\left[\frac{\partial u_i'}{\partial t} + \frac{\partial}{\partial y_k}(u_i'u_k')\right] = \int_{V_{fl\infty}} g(\mathbf{x}-\mathbf{y})\frac{\partial T_{ik}'}{\partial y_k}dV_y + \\ \rho_{fl}g_i\int_{V_{fl\infty}} g(\mathbf{x}-\mathbf{y})dV_y.\end{aligned} \tag{A15}$$

By examining Eq. A3, one immediately obtains $\rho_{fl}g\int_{V_{fl\infty}} g(\mathbf{x}-\mathbf{y})dV_y = \rho_{fl}g\epsilon$. Furthermore, inserting the results of Eq. A8 with $a' = u_i'u_k'$ and Eq. A10 with $a' = u_i'$ to Eq. A15 immediately produces

$$\begin{aligned}\rho_{fl}\int_{V_{fl\infty}} g(\mathbf{x}-\mathbf{y})\left[\frac{\partial u_i'}{\partial t} + \frac{\partial}{\partial y_k}(u_i'u_k')\right]dV_y = \\ \rho_{fl}\frac{\partial}{\partial t}\left[\epsilon(\mathbf{x})u_i(\mathbf{x})\right] + \rho_{fl}\frac{\partial}{\partial x_k}\int_{V_{fl\infty}} u_i'(\mathbf{y})u_k'(\mathbf{y})g(\mathbf{x}-\mathbf{y})dV_y,\end{aligned} \tag{A16}$$

where the second term in the right-hand side can be evaluated further by using the assumption made earlier: the local fluctuation in a flow quantity are due to variations on scales comparable to particle spacings and system dimensions. Accordingly, the local velocity can be expressed as $u_i' = u_i + u_i''$, where u_i'' represent the velocity fluctuations on a particle scale. Inserting this definition to the second right-hand side term in Eq. A16 leaves

$$\begin{aligned}\int_{V_{fl\infty}} u_i'(\mathbf{y})u_k'(\mathbf{y})g(\mathbf{x}-\mathbf{y})dV_y = \int_{V_{fl\infty}} u_iu_k(\mathbf{y})g(\mathbf{x}-\mathbf{y})dV_y + \\ \int_{V_{fl\infty}} (u_i''u_k + u_iu_k'')(\mathbf{y})g(\mathbf{x}-\mathbf{y})dV_y + \int_{V_{fl\infty}} u_i''u_k''(\mathbf{y})g(\mathbf{x}-\mathbf{y})dV_y.\end{aligned} \tag{A17}$$

Taking $a = u_i u_k$ and applying Eq. A3, the first term in Eq. A17 is clearly $\epsilon u_i u_k(\mathbf{x})$. Furthermore, in the second term of Eq. A17, the local average values u_i and u_k vary little over distances characterized by g and can be moved outside of the integral. Since the contributions of u_i'' and u_k'' in the second term integral can be expected to contribute very little, the second term of Eq. A17 can be ignored alltogether. Finally, the left-hand side of Eq. A15 can be expressed conveniently as [24]

$$\begin{aligned}\rho_{fl}\int_{V_{fl\infty}} g(\mathbf{x}-\mathbf{y})\left[\frac{\partial u_i'}{\partial t}+\frac{\partial}{\partial y_k}(u_i'u_k')\right] = \\ \rho_{fl}\left[\frac{\partial}{\partial t}(\epsilon(\mathbf{x},t)u_i(\mathbf{x},t))+\frac{\partial}{\partial x_k}(\epsilon u_i u_k(\mathbf{x}))\right]+\frac{\partial R_{ik}}{\partial x_k},\end{aligned} \tag{A18}$$

where $R_{ik} = \rho_{fl}\int_{V_{fl\infty}} u_i'' u_k''(\mathbf{y}) g(\mathbf{x}-\mathbf{y}) dV_y$.

Now, returning to the right-hand side of Eq. A15, we can apply Eq. A8 with $a' = T_{ik}'$ resulting in

$$\begin{aligned}\int_{V_{fl\infty}} g(\mathbf{x}-\mathbf{y})\frac{\partial T_{ik}}{\partial y_k}dV_y = \frac{\partial}{\partial x_k}\left[\epsilon T_{ik}(\mathbf{x})\right] - \\ \sum_{p\infty}\int_{s_p} n_k T_{ik}'(\mathbf{y}) g(\mathbf{x}-\mathbf{y}) dS_y,\end{aligned} \tag{A19}$$

where, again decomposing the Cauchy stress tensor to $T_{ik}' = T_{ik} + T_{ik}''$ yields

$$\begin{aligned}\int_{V_{fl\infty}} g(\mathbf{x}-\mathbf{y})\frac{\partial T_{ik}'}{\partial y_k}dV_y = \frac{\partial}{\partial x_k}\left[\epsilon T_{ik}(\mathbf{x})\right] - \sum_{p\infty}\int_{s_p} n_k T_{ik}(\mathbf{y}) g(\mathbf{x}-\mathbf{y}) dS_y - \\ \sum_{p\infty}\int_{s_p} n_k T_{ik}''(\mathbf{y}) g(\mathbf{x}-\mathbf{y}) dS_y,\end{aligned} \tag{A20}$$

where applying Eq. A4 to the second right-hand side term equals to [24]

$$\begin{aligned}\sum_{p\infty}\int_{s_p} n_k T_{ik}(\mathbf{y}) g(\mathbf{x}-\mathbf{y}) dS_y = \sum_{p\infty}\int_{v_p}\frac{\partial}{\partial y_k}\left[T_{ik}(\mathbf{y})g(\mathbf{x}-\mathbf{y})\right]dV_y = \\ \int_{V_{s\infty}}\frac{\partial}{\partial y_k}\left[T_{ik}(\mathbf{y})g(\mathbf{x}-\mathbf{y})\right]dV_y = \int_{V_{s\infty}} g(\mathbf{x}-\mathbf{y})\frac{\partial T_{ik}}{\partial y_k}dV_y - \\ \frac{\partial}{\partial x_k}\int_{V_{s\infty}} T_{ik}(\mathbf{y}) g(\mathbf{x}-\mathbf{y}) dV_y,\end{aligned} \tag{A21}$$

where Eq. A6 has been applied to the second term on the right-hand side. Furthermore, it should be stressed that here, the integration is over the volume of the particles, $\int_{V_{s\infty}} g(\mathbf{x}-\mathbf{y})dV_y = 1-\epsilon(\mathbf{x})$. Now, since both T_{ik} and $\partial T_{ik}/\partial y_k$ are expected to vary very little over the distances comparable to the radius of g, they can be taken outside the integrals and evaluated at $\mathbf{x}$. Thus, Eq. A21 reduces to [24]

$$\begin{aligned}\int_{V_{s\infty}}\frac{\partial}{\partial y_k}\left[T_{ik}(\mathbf{y})g(\mathbf{x}-\mathbf{y})\right]dV_y = \frac{\partial T_{ik}(\mathbf{x})}{\partial x_k}\left[1-\epsilon(\mathbf{x})\right] - \\ \frac{\partial}{\partial x_k}\left[T_{ik}(\mathbf{x})(1-\epsilon(\mathbf{x}))\right] = T_{ik}(\mathbf{x})\frac{\partial\epsilon(\mathbf{x})}{\partial x_k}.\end{aligned} \tag{A22}$$

Inserting this result to Eq. A20 clearly leaves [24]

$$\int_{V_{fl\infty}} g(\mathbf{x}-\mathbf{y})\frac{\partial T'_{ik}}{\partial y_k}dV_y = \epsilon(\mathbf{x})\frac{\partial T_{ik}(\mathbf{x})}{\partial x_k} - \sum_{p\infty}\int_{s_p} n_k T''_{ik}(\mathbf{y})g(\mathbf{x}-\mathbf{y})dS_y, \tag{A23}$$

where ignoring the variations of g over distances corresponding to particle diameters allows for the final form of the second right-hand side term [24]

$$\sum_{p\infty}\int_{s_p} n_k T''_{ik}(\mathbf{y})g(\mathbf{x}-\mathbf{y})dS_y = \sum_{p\infty} g(\mathbf{x}-\mathbf{x_m})\int_{s_p} n_k T''_{ik}dS_y, \tag{A24}$$

where $\mathbf{x_m}$ corresponds to the centre of mass of an individual particle. With reasonable mathematical assumptions, this expressions equals to [24]

$$\sum_{p\infty} g(\mathbf{x}-\mathbf{x_m})\int_{s_p} T''_{ik}n_k dS = n(\mathbf{x})f_i(\mathbf{x}) - [1-\epsilon(\mathbf{x})]\frac{\partial T_{ik}}{\partial x_k}, \tag{A25}$$

where n is the number of particles per volume and f_i is the average force imposed by the fluid on an individual particle. Finally, collecting the results of Eqs. A25, A23 and A18 together yields the compact form of the second Navier-Stokes equation expressed in terms of local average quantities [24]

$$\rho_{fl}\epsilon\left[\frac{\partial u_i}{\partial t} + u_k\frac{\partial u_i}{\partial x_k}\right] = \frac{\partial \Lambda_{ik}}{\partial x_k} - nf_i + \epsilon\rho_{fl}g_i, \tag{A26}$$

where $\Lambda_{ik} = T_{ik} - R_{ik}$. Additionally, if the Reynolds number is small, the flow can be deemed laminar [63], and $\Lambda_{ik} = T_{ik}$. Accordingly, Eq. A26 is expressed in compact form as

$$\rho_{fl}\epsilon_{fl}\left[\frac{\partial \mathbf{u}}{\partial t} + \nabla\cdot(\mathbf{uu})\right] = \nabla\cdot\mathbb{T}_k - n\mathbf{f} + \rho_{fl}\epsilon_{fl}\mathbf{g}, \tag{A27}$$

where the vector quantities now denote the local mean quantities.

B The drag force models

The three drag force models considered here differ primarily on the manner in which they were originally conceived. Each of these models attempts to accommodate the presence of the surrounding particles, which is reflected in these models as the drag force depends on the solid and volume fluid fractions (ϵ_s, ϵ_{fl}), as well as the relative velocity between the particle and the fluid the particle is embedded in.

In the earlier work of Ergun and Wen *et al.*, the drag force was obtained by empirically measuring the pressure drop over a packed bed consisting of numerous materials [64]. They obtained [65]

$$\mathbf{f}_d = \beta\left(\mathbf{v}+\mathbf{u}\right), \tag{B1}$$

where β was defined as [65]

$$\beta_{Ergun} = 150\frac{{\epsilon_s}^2\eta}{\epsilon_{fl}d_p^2} + 1.75\frac{\epsilon_s\rho_s}{d_p}|\mathbf{v}-\mathbf{u}|, \epsilon_{fl} < 0.8 \tag{B2a}$$

$$\beta_{Wen-Yu} = \frac{3}{4}C_D\frac{\epsilon_s\rho_s}{d_p}|\mathbf{v}-\mathbf{u}|\epsilon_{fl}^{-2.65}, \epsilon_{fl} \geq 0.8, \tag{B2b}$$

where η denotes the fluid viscosity and d_p is the particle diameter. Furthermore, C_D equals to [65]

$$C_D = \frac{24}{\epsilon_{fl}}\left[1 + 0.15\left(\epsilon_{fl}Re_p\right)^{0.687}\right], Re_p < 1000 \tag{B3a}$$

$$C_D = 0.44, Re_p \gg 1000 \tag{B3b}$$

where Re_p refers to the particle Reynolds number, which is a dimensionless parameter describing the relation between inertial and viscous forces with regards to the particle [66]. The formal definition is [65]

$$Re_p = \frac{\rho_{fl}d_p|\mathbf{v}-\mathbf{u}|}{\eta}. \tag{B4}$$

On the other hand, this model performs best with large granular packing fractions ϵ_s [64]. Based on experimental data, Di Felice proposed an improved model, where the presence of surrounding particles (packing fraction) is accounted for more carefully, which translates into an altered form for β. Thus, the value of β is described by [65]

$$\beta = \frac{3}{4}C_D\frac{\epsilon_s\rho_{fl}}{d_p}|\mathbf{v}-\mathbf{u}|f(\epsilon_{fl}), \tag{B5}$$

where the function $f(\epsilon_{fl})$ is formally expressed as [65]

$$f(\epsilon_{fl}) = \epsilon_{fl}^{-x}. \tag{B6}$$

The exponent x in the expression above is dependent on the particle Reynolds number Re_p [65]

$$x = 3.7 - 0.65\exp\left[-\frac{1}{2}\left(1.5 - \log_{10}Re_p\right)^2\right], \tag{B7}$$

while C_D is formally stated as [65]

$$C_D = \left(0.63 + \frac{4.8}{\sqrt{Re_p}}\right)^2. \tag{B8}$$

Finally, more recent simulations based on the lattice-Boltzmann method have indicated, that the Ergun model provides erroneous values for the drag force in the intermediate-high Re_p range. Therefore, using data from these simulations, Koch and Hill obtained an empirical estimate for the drag force. This reads [21, 46]

$$\mathbf{f}_d = F_0(\epsilon_s) + F_1(\epsilon_s)Re_p^2, Re_p < 20, \tag{B9a}$$

$$\mathbf{f}_d = F_0(\epsilon_s) + F_3(\epsilon_s)Re_p^2, Re_p > 20 \tag{B9b}$$

where F_0 is formally expressed as [46]

$$F_0 = \frac{1 + 3\left(\frac{\epsilon_s}{2}\right)^{1/2} + \left(\frac{135}{64}\right)\epsilon_s \ln \epsilon_s + 16.14\epsilon_s}{1 + 0.681\epsilon_s - 8.48{\epsilon_s}^2 + 8.16{\epsilon_s}^3}, \tag{B10}$$

and F_1 [21]

$$F_1 = 0.110 + 5.10 \cdot 10^{-4} \exp(11.6\epsilon_s), \tag{B11}$$

while F_3 equals to [46]

$$F_3 = 0.0673 + 0.212\epsilon_s + \frac{0.0232}{1 - {\epsilon_s}^5}. \tag{B12}$$

It should therefore be apparent, that the Di Felice and the Koch-Hill forms of the drag force represent gradual improvements to the original work by Ergun. Additionally, since in this work, laminar flow conditions can be assumed (low Re_p) in the vicinity of the hopper orifice, both the Di Felice and the Koch-Hill models should yield similar results.